Bell Test of Quantum Entanglement in Attosecond Photoionization

Marco Ruberti,[1,2,*] Vitali Averbukh,[1] and Florian Mintert[1,3]
[1]*Quantum Optics and Laser Science Group, Physics Department, Imperial College London, London, SW7 2BW, United Kingdom*
[2]*Max Born Institute for Nonlinear Optics and Short Pulse Spectroscopy, Max-Born-Straße 2A, 12489 Berlin, Germany*
[3]*Helmholtz-Zentrum Dresden-Rossendorf, Bautzner Landstraße 400, 01328 Dresden, Germany*

(Received 12 January 2024; accepted 7 October 2024; published 13 November 2024)

Attosecond physics enables the study of ultrafast coherent electron dynamics in matter upon photoexcitation and photoionization, revealing spectacular effects such as hole migration and coherent Auger dynamics in molecules. In the photoionization scenario, there has been a strong focus on probing the physical manifestations of internal quantum coherence within the individual parent ion and photoelectron systems. However, quantum correlations between these two subsystems emerging from attosecond photoionization events have thus far remained much more elusive. In this work, we design theoretically and model numerically a direct probe of quantum entanglement in attosecond photoionization in the form of a Bell test. We simulate from first principles a Bell test protocol for the case of noble gas atoms photoionized by ultrashort, circularly polarized infrared laser pulses in the strong-field regime predicting robust violation of the Bell inequality. This theoretical result paves the way for the direct observation of entanglement in the context of ultrafast photoionization of many-electron systems. Our work provides a novel perspective on attosecond physics directed toward the detection of quantum correlations between systems born during attosecond photoionization and unraveling the signatures of entanglement in ultrafast coherent molecular dynamics, including in the chemical decomposition pathways of molecular ions.

DOI: 10.1103/PhysRevX.14.041042

Subject Areas: Atomic and Molecular Physics, Quantum Physics, Quantum Information

I. INTRODUCTION

Entanglement is one of the most iconic manifestations of the laws of quantum mechanics. It is a type of correlation between different constituents of a quantum system that has no real analog in classical physics [1], and it is a key ingredient for quantum information science [2], where it can be used as a resource for quantum computation, metrology, and imaging [1–6]. Quantum entanglement has also received much attention in the context of atomic and molecular physics, with particular focus on the properties of the emitted entangled photons [7–9]. However, the role played by quantum entanglement in the electron dynamics in atoms and molecules remains largely unexplored, and its effect on the physical processes occurring on the natural electronic, i.e., attosecond, timescale is yet to be understood.

The main goal of attosecond physics is to resolve ultrafast electron dynamics in a wide variety of atomic, molecular, and condensed phase systems [10]. Following the spectacular advances in the synthesis and characterization of ultrashort laser pulses [11,12], of time duration ranging from a few tens of femtoseconds down to hundreds of attoseconds, a large variety of spectroscopic and imaging techniques reaching attosecond time resolution have been developed including methods based on strong-field light-matter interaction such as high-order harmonic generation (HHG) spectroscopy [13], laser-induced electron diffraction [14], photoelectron holography [15] attosecond streaking [16], and attosecond pump-probe spectroscopy [17–19]. The key physical process that lies in the basis of these techniques, whether relying on HHG sources [20] or on x-ray free-electron lasers [21], is photoionization. While photoionization is certainly one of the universally acknowledged manifestations of the quantum nature of matter that led, for example, to the discovery of energy quanta, it is far less widely appreciated that it also bears the mark of quantum entanglement [22–28].

During the photoionization process, an originally bound many-electron quantum system, such as an atom or a molecule, is broken up, in the simplest scenario, into two

*Contact author: m.ruberti11@imperial.ac.uk

Published by the American Physical Society under the terms of the Creative Commons Attribution 4.0 International license. Further distribution of this work must maintain attribution to the author(s) and the published article's title, journal citation, and DOI.

subsystems: the emitted photoelectron and its parent ion. In the cases where, for example, the parent ion can be found in multiple quantum states, one can expect such multichannel photoionization to result in an entangled state of the photoelectron and the ion, in which neither of the produced spatially separated particles can be assigned particular values of the physical observables, such as energy, angular momentum, or spin. The most immediate consequence of the presence of entanglement between the photoelectron and the parent ion upon photoionization is that each subsystem is in general characterized by a mixed quantum state possessing a reduced degree of internal quantum coherence [25,29–31]. A pioneering work was able to demonstrate reduced coherence of the ionic system by theoretically predicting and experimentally characterizing the density matrix of atomic krypton ions emerging from strong-field ionization [25], while experimental reconstruction of the photoelectron density matrix upon atomic photoionization has also been reported more recently [32].

However, the emerging picture of the interplay of coherence and entanglement in photoionization has so far not been supported by any quantitative measurement of quantum entanglement, and no procedure for such a measurement has been proposed. Indeed, the common description of ultrafast photoionization experiments has concentrated on the internal, ultrafast dynamics that is underpinned by the quantum coherence within each of the subsystem produced by photoionization, such as hole migration [19] in the ion, while the quantum correlations between the photoelectron and the parent ion have remained elusive in attosecond physics.

The majority of studies of photoionization and the ensuing electron processes have treated the parent ion and photoelectron as if they were individual, isolated systems, i.e., fully neglecting their mutual quantum correlations. One example of such an approach is provided by the bulk of theoretical work on hole migration following photoionization of polyatomic molecules, including small biomolecules [33–39]. In these works, the so-called sudden approximation is invoked to approximate, in the limit of large photon energy, the state of the parent ion as a pure, coherent superposition of energy eigenstates, which is predicted to feature a migration of the positive charge across the backbone of the molecular ion on a sub- to few-femtosecond timescale [33]. The sudden approximation picture explicitly neglects the effect of the entanglement between the photoelectron and the molecular cation. In a similar way, the majority of studies aiming to characterize photo and secondary (e.g., Auger) electrons neglected the entanglement between the emitted photoelectron and the parent ion or between the photoelectron and Auger electron in the postcollision interaction scenario, where the energy exchange between the two consecutively emitted particles has been treated semiclassically [40–42].

Nevertheless, already in an early work [43] it was realized that measurement of the entire set of observables for the photoelectron only is not sufficient to obtain a complete characterization of an inner-shell photoionization process [43], and that additional information about the atomic cation is needed [44]. This was clearly indicating the presence of correlations between the two subsystems, even though their nature, classical or quantum, was not revealed then yet. Moreover, starting from the early 2000s, a few studies have explored the role of entanglement in attosecond processes. Some of these works have focused on entanglement between the photoelectron and the parent ion [26–29,31,45–56], while other studies have focused on electron-electron entanglement [57–60]. A pioneering experimental work [24] has been able to probe hole localization after inner-shell ionization of molecular nitrogen by measuring in coincidence the ultrafast Auger electron angular emission patterns and the spectrum of nuclear fragments. The results showed that observation of symmetry breaking (electronic hole localization) or preservation (electronic hole delocalization) depends on how the quantum entangled Bell state created by Auger decay is detected by measurement. More recently, experimental investigations of ultrafast preparation of atomic Bell-like states [61], as well as of ultrafast control mechanisms for vibrational and electronic entanglement [27,28,62], have also been performed. However, these studies have investigated photoelectron-ion entanglement in an indirect way, mostly by monitoring the change of internal quantum coherence in one of the entangled subsystems [27,28,54,55]. A direct test for quantum entanglement is given by verifying the violation of Bell inequalities [63–67]. If applied to photoionization, the Bell test should be, in its simplest realization, based on detecting correlations in the measurements of two noncommuting observables for both the parent ion and the photoelectron. Such a direct and rigorous verification and quantification of the quantum entanglement produced upon photoionization are still missing, and direct experimental evidence of this type of entanglement has so far been considered to be "often practically impossible, requiring the measurement of incompatible observables, such as momentum and position" [60].

In this work, we conceptually design and numerically simulate a Bell test experiment for the case of atomic photoionization. Specifically, we consider argon atoms photoionized by ultrashort, circularly polarized infrared (IR) laser pulses in the strong-field regime. We derive Bell inequalities that are sensitive to the entanglement between the atomic ion internal degrees of freedom and the photoelectron spin. We show that by exploiting the spin polarization of the photoelectron beam, one can observe a robust violation of the Bell inequalities, demonstrating quantum entanglement between the photoelectron and the atomic ion. Our results demonstrate a quantum protocol for rigorous detection of quantum entanglement in ultrafast photoionization and pave the way to the direct observation of entanglement in the context of attosecond physics.

II. PROTOCOL FOR DESIGNING A BELL TEST

A. Choice of Bell inequality type and photoelectron observables

In order to verify and quantify the entanglement between the photoelectron and its parent ion, it is necessary to perform coincidence measurements on the two subsystems. In this type of measurement setup, the quantum correlations are reflected by the coincidence statistics, which are sensitive to which observables of the emitted photoelectron and its parent ion are measured.

In this work, we construct Bell inequalities of the Clauser-Horne-Shimony-Holt (CHSH) type [68], which require the measurement of two different noncommuting observables per subsystem. This type of Bell inequality is based on dichotomic observables, i.e., on observables adopting only two values, which can be arbitrarily set equal to ± 1. The most common Bell test for a pair of entangled particles requires the evaluation, in separate experiments, of the quantity $\mathbb{S}$ combining four quantum correlation functions of the particles pair in the following way:

$$\mathbb{S} = \langle \hat{A}(a) \otimes \hat{B}(b) \rangle - \langle \hat{A}(a) \otimes \hat{B}(b') \rangle + \langle \hat{A}(a') \otimes \hat{B}(b) \rangle + \langle \hat{A}(a') \otimes \hat{B}(b') \rangle, \quad (1)$$

where a, a' and b, b' denote different settings for the detector of particle A and of particle B, respectively. Violations of the CHSH inequality, i.e., $\mathbb{S} > 2$, are predicted for entangled states by the laws of quantum mechanics, which also set a maximum value for the value of $\mathbb{S}$ of $2\sqrt{2}$ known as Tsirelson's bound [69].

A key step to design a Bell test of the CHSH type consists of correctly identifying the appropriate pairs of noncommuting observables to be measured for each subsystem. In the case of a free photoelectron resulting from a photoionization event, the set of observables that could in principle be measured consists of its kinetic energy ξ, its linear orbital momentum (angle of emission) or orbital angular momentum, and its spin angular momentum. As a result of photoionization, the entanglement between the photoelectron and the cation can in principle be encoded in each of these different degrees of freedom of the photoelectron.

Among all the possible corresponding observables, the kinetic energy is not a good one for entanglement tests because it commutes with all the other photoelectron observables. On the contrary, Bell inequalities can in principle be constructed using different, noncommuting components of either the orbital or the spin angular momentum of the free photoelectron. In general, components of the two angular momenta, as well as noncommuting components of linear and angular momenta of the free photoelectron, are also potentially good candidates to construct a Bell test.

Despite recent progress in measuring the orbital angular momentum of electron beams, as demonstrated in Refs. [70–72], this observable remains, in general, difficult to measure with high accuracy, and its detection is still affected by considerable experimental error [70–72]. However, there exist established techniques that allow one to accurately measure the spin projection of a free electron along any direction in space.

The spin degree of freedom of photoelectrons has been measured with a Mott detector [73,74] in order to determine the spin polarization resulting from strong-field ionization with circularly polarized light. Such a detector relies on spin-orbit interactions and the consequent spin-dependent asymmetry in the scattering of electrons at high-Z atoms. Retarding-potential Mott polarimeters have also been used to perform single-particle-resolved measurements of electron spin and spin coincidence measurements of scattered electron pairs [75]. The main limiting factor in spin measurements based on Mott scattering experiments is the low cross section for spin-orbit scattering and the resulting poor detection efficiency. In fact, the typical Mott detector efficiency reported in the literature is approximately 2×10^{-4} [76].

However, other approaches have been developed and successfully applied over the last two decades. These approaches exploit the exchange interaction between low-energy (a few tens of eV) photoelectrons and magnetically ordered target surfaces in low-energy electron-diffraction- (LEED) like reflectometry geometries [77], leading to an increase in efficiency by a factor of 10^2 with respect to the Mott detector and, therefore, rendering the spin detection suitable for high-resolution angular-resolved photoelectron energy distributions (ARPES) [78–82]. As an example of combined spin and ARPES detection, a state-of-the-art spin-ARPES spectrometer is available as a users' station at the Elettra synchrotron radiation facility in Trieste (Italy) [78]. This spectrometer employs an optimized three-dimensional vectorial spin polarimeter, it has an efficiency of 3.3×10^{-2}, and allows for three-dimensional spin-vector measurements of high-energy and momentum-resolved ARPES data.

To date, setups based on the LEED spin detection method can operate with a 10^{-2} efficiency for specific ranges of the kinetic energy of the electron, depending on the type of surface used. For example, in Ref. [81] several optimal efficiency ranges of up to 12 eV width were demonstrated within the photoelectron energy range relevant to this work. In addition, it is possible to accelerate or decelerate the photoelectron to the optimal kinetic energy.

B. The target system and photoionization regime: The case of noble gas atoms photoionized by circularly polarized light

Following the considerations of Sec. II A, in this work we will explore an entanglement test based on the

observation of the spin angular momentum of the photoelectron. Therefore, the pair of noncommuting operators $\hat{B}(b)$ and $\hat{B}(b')$ [see Eq. (1)] for the photoelectron subsystem will be $2\hat{S}_{r_i}$ and $2\hat{S}_{r_j}$, where r_i and r_j denote two nonparallel directions in space, and the factor of 2 is required for the above operators to have eigenvalues equal to ± 1. This type of test requires quantum entanglement to be encoded in the spin degree of freedom of the photoelectron. The aforementioned condition can be achieved, for example, by photoionization of noble gas atoms with intense, circularly polarized IR laser pulses under standard experimental conditions. Indeed, it was both predicted theoretically [83,84], and verified experimentally [73,74,85,86], that this type of ionization process gives rise to photoelectron beams characterized by a high degree of spin polarization. Previous analytical calculations also predicted the polarization of the photoelectron beam to depend on the specific ionization channel [74,83], which reflects the entanglement between the internal spin-orbit states of the parent ion and the projection of the emitted electron's spin along the propagation direction of the ionizing laser beam. Spin polarization arises due to the interplay of the electron-ion entanglement and the strong dependence, in intense circularly polarized fields, of the ionization probability on the sense of electron rotation in the initial state, i.e., on the sign of the magnetic quantum number m_l of the orbital the electron is removed from, relative to the sense of rotation of the ionizing circularly polarized field. Since, especially for low photoelectron energies, the probability of ionization from a corotating orbital is much lower than from a counterrotating one, the low-energy photoelectron emission is strongly spin polarized via suppression of emission of corotating electrons [73,74,83–86]. Here it is important to note that, even though in the present work we focus on the case of noble gas atoms' strong field ionized by circularly polarized IR pulses, the entanglement protocol that we construct is by no means restricted to such regimes. Other photoionization regimes that feature in spin polarization of the photoelectron beam include single-photon ionization, either from a particular fine-structure level of an atom or a molecule [87] or in the vicinity of the Cooper minima in the photoionization continua [88], and resonant multiphoton ionization in the perturbative limit [89,90]. Importantly, a high degree of spin polarization (close to 100%) is not always associated with minima in cross sections, but can be achieved, e.g., away from the minimum in the three-photon ionization cross section of alkali-metal atoms [91] and at the maximum of the one-photon cross section for Xe [92].

In the scheme presented here, the many-electron system considered consists of a neutral N-electron atom that is initially, i.e., before photoionization, in its electronic ground state $|\Psi_N^0\rangle$. The states of the parent ion that are populated by the photoionization process and that are relevant for the measurement protocol proposed here are shown in Fig. 1. The yield of different ionization channels in strong-field ionization (SFI) depends exponentially on their respective ionization potential. Therefore, in the case of Ar^+ only the two lowest energy levels $^2P_{3/2}$ and $^2P_{1/2}$ are effectively populated upon photoionization. The spin-orbit splitting of these two energy levels is $\Delta E = 0.1775$ eV, with an ionization potential of the parent

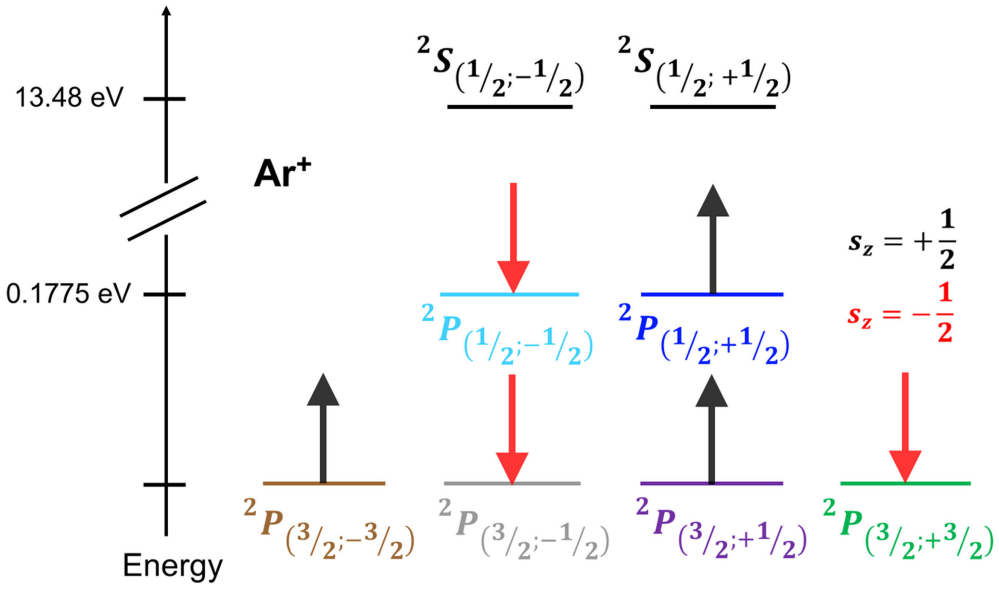


FIG. 1. Energy levels of Ar^+ parent ion. In the bottom part of the figure, the fourfold-degenerate ground state $^2P_{3/2}$, and the twofold-degenerate first excited state $^2P_{1/2}$, which are populated upon strong-field ionization by circularly polarized IR laser pulses, are shown. The specific spin orientation, along the propagation direction of the ionizing laser pulse, of the correspondent photoelectron is also shown. The second, higher-lying, excited state $^2S_{1/2}$ is also shown.

ion ground state $^2P_{3/2}$ equal to $I_P = 15.75962$ eV. The ionization potential of the second excited state $^2S_{1/2}$ of Ar^+ is much higher (29.24394 eV), and therefore the population of this state upon SFI can be safely neglected. SFI of p_0 electrons by circularly polarized light is strongly suppressed and will be neglected here. Both approximations are fully justified based on previous analytical calculations [83], and the high accuracy of this approximation has been confirmed by the results of the *ab initio* simulations performed in this work, as we will show in Sec. III B.

As a result of photoionization dynamics and of the coupling of the spin and orbital angular momenta as given by the Clebsch-Gordan coefficients, a single specific spin state of the photoelectron corresponds to each ionization channel. This is illustrated in Fig. 1. Thus, the complete photoionized state can be written as

$$|\Psi_N^F\rangle = \sum_{j=1}^{6} \iint d\xi d\alpha\, C_{js_j}(\xi,\alpha)|^2P_{l_jm_j};\xi s_j\alpha\rangle, \quad (2)$$

with $s_1 = s_3 = s_6 = \uparrow$, $s_2 = s_4 = s_5 = \downarrow$, $l_1 = l_4 = 1/2$, $l_2 = l_3 = l_5 = l_6 = 3/2$, $m_2 = 3/2$, $m_1 = m_3 = 1/2$, $m_4 = m_5 = -1/2$, $m_6 = -3/2$, where the photoelectron is described by its kinetic energy ξ, the value of its spin component along the propagation direction of the photoionizing pulse $\uparrow/\downarrow$, and any extra degree of freedom denoted by α, e.g., $\alpha = (l, m)$ or $\alpha = (\theta, \phi)$.

The spin polarization Pol_S of the photoelectron emitted from the $^2P_{3/2}$ and $^2P_{1/2}$ channels is defined as

$$\mathrm{Pol}_S^{^2P_{3/2}} = \frac{\sum_j^{3,6}|C_{j\uparrow}(\xi,\alpha)|^2 - \sum_j^{2,5}|C_{j\downarrow}(\xi,\alpha)|^2}{\sum_j^{2,3,5,6}|C_{js_j}(\xi,\alpha)|^2},$$
$$\mathrm{Pol}_S^{^2P_{1/2}} = \frac{|C_{1\uparrow}(\xi,\alpha)|^2 - |C_{4\downarrow}(\xi,\alpha)|^2}{\sum_j^{1,4}|C_{js_j}(\xi,\alpha)|^2}. \quad (3)$$

The values that the channel-resolved spin polarization can reach along the propagation direction of the photoionizing laser pulse are $\mp 50\%$ and $\pm 100\%$ for the fourfold-degenerate $^2P_{3/2}$ and the twofold-degenerate $^2P_{1/2}$ ionization channels, respectively. In order to approach such strong spin polarizations, it is necessary to suppress ionization from the corotating atomic orbital and mainly have emission of electrons from the counterrotating atomic orbital [85,93,94]. In particular, the ionic states with positive M_J (i.e., $|^2P_{1/2,+1/2}\rangle$, $|^2P_{3/2,+3/2}\rangle$, and $|^2P_{3/2,+1/2}\rangle$) or negative M_J can be predominantly populated depending on the handedness of the circularly polarized field, i.e., onto whether the counterrotating orbital is the p_{-1} or the p_{+1}, respectively.

Moreover, to obtain a significant level of entanglement in the photoionized state, it is necessary for the ionization yields corresponding to the two energy channels of the parent ion, separated in energy by the ground-state spin-orbit splitting, to have comparable values. As will be shown in the next section, this requirement will be fully satisfied in the case of Ar^+.

C. Choice of observables for the cation and formulation of the Bell inequality

Finally, in order to design a Bell test, it is necessary to identify the choice of the pair of noncommuting operators [$\hat{A}(a)$ and $\hat{A}(a')$; see Eq. (1)] for the ionic subsystem that will result in the clearest verification of entanglement, i.e., in the strongest violation of the Bell inequality, for the states resulting from photoionization. This pair of ionic operators will be denoted $\hat{Q}^{\mathrm{Ion}}$ and $\hat{R}^{\mathrm{Ion}}$ from here on in this work.

Direct, projective measurements on the parent ion can be concretely realized in the basis of its energy eigenstates. Since this basis typically does not coincide with measurement bases that are required for the Bell test, it is necessary to drive transitions in the ion that map the physically available measurement basis to the measurement bases that are required for the Bell test. Therefore, in order to construct a pair of noncommunting ionic operators $\hat{Q}^{\mathrm{Ion}}$ and $\hat{R}^{\mathrm{Ion}}$, the measurement in the ionic eigenbasis is combined with additional coherent dynamics that is driven in the parent ion system with control laser pulses, and it is described by the unitary operators $\hat{U}_Q$ and $\hat{U}_R$, respectively. Measuring an observable $\hat{O}$, which is diagonal in the ionic eigenbasis, after the coherent evolution $\hat{U}_Q$ amounts to measuring the observable

$$\hat{Q}^{\mathrm{Ion}} = \hat{U}_Q^\dagger \hat{O} \hat{U}_Q, \quad (4)$$

and similarly for $\hat{R}^{\mathrm{Ion}}$. Analogously to the noncommuting spin observables for the photoelectron subsystem $\hat{S}_{r_i,r_j}$ that are also unitary transformations of each other, the two ionic observables created via two unitary transformations of the diagonal observable $\hat{O}$ generally do not commute with each other and can therefore be used in a Bell test.

Quantum-state manipulation through coherent interaction with a radiation field is a fundamental process with a wide variety of implementations in quantum optics and quantum information processing [2,95]. The control pulse scheme that we propose in this work, and the corresponding Hamiltonian matrix elements between the ionic states involved, are schematically illustrated in Figs. 2 and 3, respectively. As can be seen in Fig. 2, the geometry of the experiment we propose is the following: The propagation direction of the circularly polarized, photoionizing IR beam is chosen along the z axis; consequently, the photoionizing field vector lies on the x-y plane. After photoionization, we propose to use two subsequent, linearly polarized control

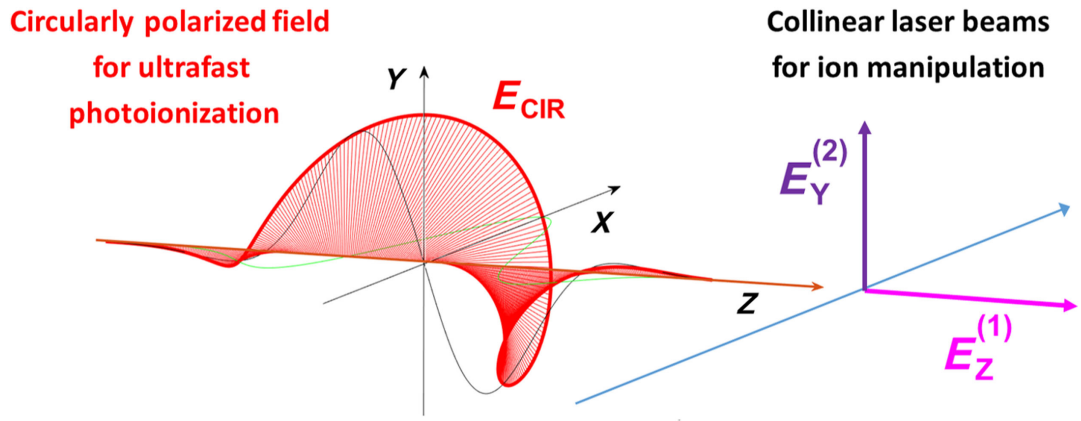


FIG. 2. Representation of the laser-pulse scheme for entanglement detection upon photoionization. The ultrashort photoionizing pulse propagates along the z axis, and its electric field is circularly polarized in the x-y plane. After photoionization, a subsequent pair of resonant laser pulses is applied, within the entanglement detection protocol, to the Ar^+ parent ion subsystem. In particular, two collinear laser beams propagating in a direction (e.g., x axis) perpendicular to the propagation direction of the photoionizing pulse are used: One laser beam has its electric field (magenta) linearly polarized along the propagation direction (z axis) of the photoionizing pulse; the second linearly polarized electric field (violet) is polarized along a perpendicular direction (e.g., y axis).

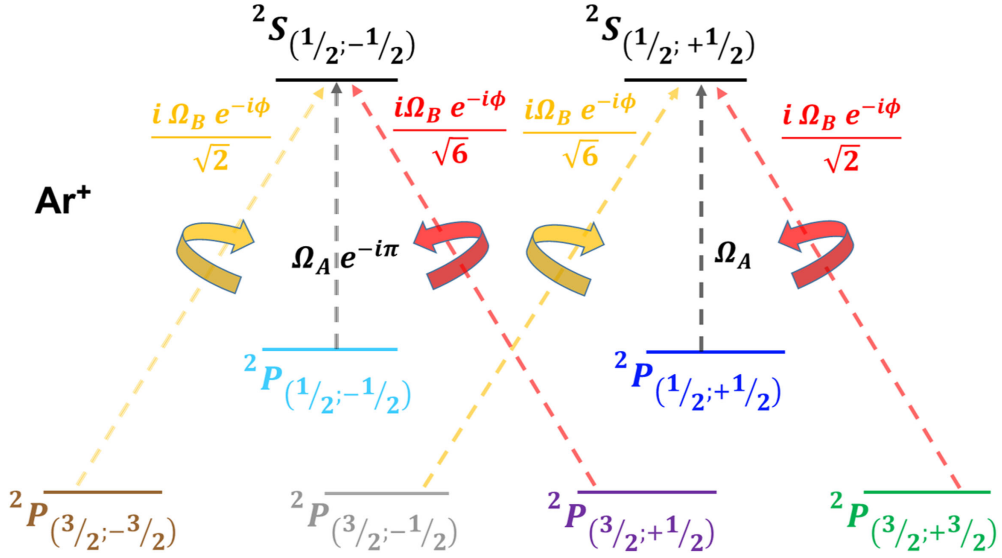


FIG. 3. Schematic representation of the couplings induced between the states of the Ar^+ parent ion subsystem by the laser pulses applied to the cation within the entanglement detection protocol. Two collinear laser beams are used with linearly polarized fields that resonantly couple the initially populated ground $^2P_{3/2}$ and first excited $^2P_{1/2}$ states to the initially unpopulated second excited state $^2S_{1/2}$. The two electric fields are linearly polarized along perpendicular directions: The one that is linearly polarized along the propagation direction of the photoionizing pulse couples states with the same value of M_J (black dashed lines); the one that is linearly polarized along a perpendicular direction (e.g., y axis) couples states with different values (± 1) of M_J. In the figure, the couplings induced by the right-handed (red dashed lines) and left-handed (orange dashed lines) circularly polarized components of the latter electric field are indicated. For every coupling, the corresponding Hamiltonian matrix elements are also shown; Ω_a and Ω_b are the Rabi frequencies and ϕ is the phase difference of the two light fields.

laser pulses that copropagate along a direction (y axis) perpendicular to the propagation axis of the IR photoionizing pulse itself; the two collinear control laser beams are synchronized with one another, and they are both delayed with respect to the photoionizing pulse. Both control pulses are applied to the parent ion subsystem for a total time T.

The states of the parent ion, which encode entanglement with the photoelectron, are characterized by the same (p) orbital symmetry. As a result, dipole transitions between them are symmetry forbidden by selection rules. Coherent operations can nevertheless be performed by increasing the active Hilbert space to the second excited state of S symmetry. Therefore, the two collinear control pulses are

linearly polarized along perpendicular directions: The electric field $E_z^{(1)}$ of one pulse is linearly polarized along the propagation direction of the photoionizing IR pulse (z axis), and its photon energy is in resonance with the energy gap between the first excited $^2P_{1/2}$ and the second excited $^2S_{1/2}$ ionic energy levels; the other pulse, with electric field $E_y^{(2)}$, has a linear polarization along the y axis, and it is resonant to the transition between the ground $^2P_{3/2}$ and the second excited $^2S_{1/2}$ ionic energy levels.

As shown in Fig. 3, the field $E_z^{(1)}$ (with the corresponding Rabi frequency denoted by Ω_a) couples the states $^2P_{1/2,+1/2}$ and $^2P_{1/2,-1/2}$ to $^2S_{1/2,+1/2}$ and $^2S_{1/2,-1/2}$, respectively. The coupling matrix elements corresponding to the two transitions differ by a π phase factor that originates from the $\hat{L}-\hat{S}$ coupling Clebsch-Gordan coefficients (see Appendix B for the detailed derivation). On the other hand, the $E_y^{(2)}$ linearly polarized field (with the corresponding Rabi frequency denoted by Ω_b) couples ionic states with different values of the magnetic quantum number M_J: The degenerate magnetic substates of the ground level $^2P_{3/2}$ with positive $M_J>0$ (negative $M_J<0$) are coupled to the second excited state $^2S_{1/2}$ by the right-handed σ^- (left-handed σ^+) polarization component of the incident $E_y^{(2)}$ light field. As shown in Fig. 3, the $^2P_{3/2,+3/2}$ and $^2P_{3/2,-1/2}$ states are coupled to $^2S_{1/2,+1/2}$, while the $^2P_{3/2,+1/2}$ and $^2P_{3/2,-3/2}$ states are coupled to $^2S_{1/2,-1/2}$. The matrix elements of the transitions involving $^2P_{3/2}$ states with $M_J=\pm 1/2$ (i.e., $^2P_{3/2,+1/2}$ and $^2P_{3/2,-1/2}$) differ by a factor of $(1/\sqrt{3})$ with respect to the ones involving $^2P_{3/2}$ states with $M_J=\pm 3/2$. This difference also originates from the Clebsch-Gordan coefficients describing the $\hat{L}-\hat{S}$ coupling of the $\hat{J}^2,\hat{J}_z$ eigenstates considered (see Appendix B for the detailed derivation). As a result, this choice of pulses gives rise to two independent four-level systems, namely, ($|^2P_{3/2,+3/2}\rangle$, $|^2P_{3/2,-1/2}\rangle$, $|^2P_{1/2,+1/2}\rangle$, $|^2S_{1/2,+1/2}\rangle$) and ($|^2P_{3/2,+1/2}\rangle$, $|^2P_{3/2,-3/2}\rangle$, $|^2P_{1/2,-1/2}\rangle$, $|^2S_{1/2,-1/2}\rangle$), respectively (see Fig. 3). The coherent operations designed, i.e., $\hat{U}_Q$ and $\hat{U}_R$, transfer to the $^2S_{1/2}$ second excited energy level some of the population that was initially prepared by the SFI in the $^2P_{3/2}$ ground and $^2P_{1/2}$ first excited levels.

In order to complete the design of the ionic operators to be used in the construction of the Bell inequality, we propose a dichotomic observable $\hat{O}^{\mathrm{Ion}}$,

$$\hat{O}^{\mathrm{Ion}} = +1\sum_{M_J}|^2S_{1/2,M_J}\rangle\langle^2S_{1/2,M_J}| - 1\sum_{J}^{\frac{1}{2},\frac{3}{2}}\sum_{M_J}|^2P_{J,M_J}\rangle\langle^2P_{J,M_J}| \tag{5}$$

that is diagonal in the basis of the ionic energy eigenstates, and distinguishes whether the parent ion has (measurement result $+1$) or has not (measurement result -1) been excited to the $^2S_{1/2}$ energy level after the application of our pulse scheme. The measurement of this observable can be implemented in the laboratory by, e.g., observing the fluorescence emission resulting from the population of the $^2S_{1/2}$ state. We therefore propose to construct the noncommuting ionic observables $\hat{Q}^{\mathrm{Ion}}$ and $\hat{R}^{\mathrm{Ion}}$ from the diagonal observable $\hat{O}^{\mathrm{Ion}}$ in Eq. (5) by unitary transformations [see Eq. (4)] that embody the ionic time evolution under the influence of the two collinear control laser pulses described above. This time evolution distinguishes different linear combinations of the three effectively coupled initially populated states as either as "dark" states (whose initial population is not transferred to the second excited state by the control laser pulses) or "bright" states (whose initial population is fully transferred to the second excited state). While the bright states lead to fluorescence, dark states do not. Different dark and bright states can be obtained by varying the parameters ($E_z^{(1)}$, $E_y^{(2)}$, ϕ, T) of the two laser pulses used; see Appendix B for the detailed derivation, the specific form, and dependence of the $\hat{Q}^{\mathrm{Ion}}$ and $\hat{R}^{\mathrm{Ion}}$ operators on the laser parameters used. In other words, depending on the values of the control laser parameters, the ionic manipulation maps different linear combinations of ionic eigenstates into dark and bright states; this is equivalent to providing different basis sets for the ionic measurement that would otherwise be not available without this mapping. As a result, the subsequent detection of fluorescence becomes formally equivalent to measurement of the noncommuting ionic observables $\hat{Q}^{\mathrm{Ion}}$ and $\hat{R}^{\mathrm{Ion}}$, as required for the Bell test.

Here it is also worth noting that the frequency of the resonant laser pulses, which need to be applied to the parent ion in order to perform these coherent operations, is sufficiently off resonance not to couple the $|^2S_{1/2}\rangle$ excited state to doubly ionized states at or above the double ionization potential of the system.

Finally, the optimal directions for the measurements of the photoelectron's spin projection $\hat{S}_{r_i,r_j}$ consist of the propagation axis of the photoionizing circularly polarized pulse (along which the photoelectron spin polarization is maximal) and a generic, orthogonal direction in the laser polarization plane. Given the geometry of Fig. 2, we thus have $\hat{S}_{r_i}=\hat{S}_z$ and $\hat{S}_{r_j}=\hat{S}_x$. Combining the measurements on the parent ion subsystem with the two independent spin measurements on the photoelectron, as given by the operators $2\hat{S}_z$ and $2\hat{S}_x$, the resultant Bell inequality reads

$$\mathbb{S} = \langle\hat{Q}^{\mathrm{Ion}}\otimes 2\hat{S}_x\rangle + \langle\hat{Q}^{\mathrm{Ion}}\otimes 2\hat{S}_z\rangle + \langle\hat{R}^{\mathrm{Ion}}\otimes 2\hat{S}_x\rangle - \langle\hat{R}^{\mathrm{Ion}}\otimes 2\hat{S}_z\rangle \geq 2. \tag{6}$$

(See Appendix B for the derivation in terms of the photoionized state coefficients). The explicit choice of the ionic operators $\hat{Q}^{\mathrm{Ion}}$ and $\hat{R}^{\mathrm{Ion}}$ should be taken based on the explicit state obtained in a photoionization process, as exemplified in more detail in Sec. III.

III. VIOLATION OF THE BELL INEQUALITY: RESULTS BY *AB INITIO* SIMULATIONS

In order to estimate the value of $\mathbb{S}$ for given ionic observables $\hat{Q}$ and $\hat{R}$, and to find observables that yield a strongly violated Bell inequality [see Eq. (6)], one needs an accurate description of the bipartite photoionized state of the photoelectron and parent ion [see Eq. (2)] produced upon SFI. In this section, this will be discussed in detail for the specific case of neutral argon.

A. *Ab initio* method and numerical parameters

The accurate, from-first-principles, prediction of the state of the full bipartite system that is produced upon multichannel photoionization on a many-electron system, and the simulation of a Bell test experiment, require the use of advanced methodologies for photoionization dynamics that can describe, on an equal footing, the bound-interacting many-electron system and the photoelectron states. In our work, we apply the advanced, *ab initio* time-dependent B-spline algebraic diagrammatic construction (ADC) method for many-electron photoionization dynamics [96–99] to compute the state coefficients in Eq. (2), as well as the populations and coherences in Eq. (B1), resulting from strong-field ionization of an argon atom.

In this work, the TD B-spline ADC method, already extensively applied to the study of attosecond many-electron dynamics in atoms and molecules [26,29,96–101], was extended by us to describe the effect of spin-orbit couplings. In particular, we have used the TD B-spline ADC approach at the first order [ADC(1)] within the ADC(n) hierarchy; we have solved the N-electron time-dependent Schrödinger equation for the argon atom interacting with the intense IR laser field given by

$$i\hbar\frac{\partial|\Psi^N(t)\rangle}{\partial t}=[\hat{H}_0+\hat{D}\cdot\mathbf{E}(t)]|\Psi^N(t)\rangle \tag{7}$$

by expressing the time-dependent state of the composite N-electron system as a linear combination of the neutral argon ground state and the manifold of one-hole–one-particle ($1h-1p$) excitations of the latter,

$$|\Psi^N(t)\rangle=C_0(t)|\Psi_0^N\rangle+\sum_{i,a}C_{i,a}(t)|\Psi_{i,a}^N\rangle. \tag{8}$$

Here the hole and particle indices corresponding to the occupied and virtual Hartree-Fock orbitals of the neutral system are indicated by i and a, respectively. In Eq. (7), $\hat{H}_0$ is the field-free N-electron ADC Hamiltonian, $\hat{D}$ is the electric dipole operator, and $\mathbf{E}(t)$ the time-dependent electric-field vector of the ionizing laser pulse.

In order to describe the effect of the spin-orbit couplings, we have worked with $1h-1p$ configurations (as well as energy eigenstates) that are eigenfunctions of the total angular momentum $\hat{J}=\hat{L}+\hat{S}$, i.e., $|\Psi_{i,a}^N\rangle=|\Psi_{i,a}^N(J,M_J,L,S)\rangle$, and we have replaced the nonrelativistic Hartree-Fock energies of the hole orbitals $\psi_i^{(j,m_j,l,s)}$ with the experimental values of the ionization potentials of the argon atom.

The B-spline ADC method at the ADC(1) level of theory has been successfully used in the strong-field regime to model the intensity-dependent interference minimum that is present in the HHG spectra of the CO_2 molecule [102]. Inclusion of the $1h-1p$ manifold in the photoionization dynamics allows one to describe the excitation of the neutral argon atom in any of the singly excited bound states as well as its photoionization into a bipartite, photoelectron, and Ar^+ system. The explicit and accurate representation of the wave function of the photoelectron is achieved by means of the B-spline single-particle basis set [96]. The time propagation of the unknown coefficients $C_{i,a}(t)$ of the N-electron state is performed by means of the Arnoldi–Lanczos algorithm [102]. We calculated the channel-resolved, energy-dependent photoelectron angular distributions and spectra in Eq. (A7) using the time-dependent surface flux technique [103].

In the simulation, we used a parabolic-linear sequence for the B-spline knots [96], a radial box radius of $R_{\mathrm{max}}=670$ atomic units, and a total of $N_b=800$ radial B-spline functions. The maximum angular momentum used in the expansion of the angular part of the photoelectron wave function in spherical harmonics was $l_{\mathrm{max}}=20$. We verified that all the results were fully converged with respect to our choice of the basis set parameters. In order to absorb the wave function and avoid its reflections from the grid boundary, we also included in the simulation a complex absorbing potential with starting radius $R_{\mathrm{abs}}=570$ atomic units.

In order to have a strong violation of the Bell inequality, the ionic states in the two $^2P_{3/2}$ and $^2P_{1/2}$ energy levels need to be populated upon photoionization as equally as possible. The relative population of the two energy levels separated by an energy gap determined by the spin-orbit splitting of the nonrelativistic ground state upon ionization strongly depends on the ionizing laser parameters (intensity and frequency) used. This dependence helps one to identify the optimal ranges of laser intensity and frequency that can potentially give rise to the strongest violation. In the simulations presented in this work, we have used an ultrashort bandwidth-limited circularly polarized laser pulse characterized by a peak intensity equal to $I_{\mathrm{peak}}=2\times10^{14}$ W/cm^2 and a central photon energy

$\hbar\omega_{\text{central}} = 2$ eV, which corresponds to a central wavelength $\lambda = 620$ nm. This pulse ejects valence $3p_{\pm1}$ electrons, leaving the residual Ar^+ ion in either the ground state $^2P_{3/2}$ or the excited state $^2P_{1/2}$, with a fine-structure splitting of about 0.1775 eV, as shown in Fig. 1. The electric field is defined such that the $l_{m_l} = p_{-1}$ electron is counterrotating (i.e., its emission is favored), and the $l_{m_l} = p_{+1}$ electron is corotating (emission suppressed).

The electric-field components in the $x - y$ plane

$$E_{\text{x}}^{\text{Cir}}(t) = E_0 \cos(\omega t) e^{-\beta(\frac{t}{\tau})^2},$$
$$E_{\text{y}}^{\text{Cir}}(t) = E_0 \sin(\omega t) e^{-\beta(\frac{t}{\tau})^2} \quad (9)$$

of the circularly polarized pulse have a Gaussian envelope with width $1/\beta$ (factor 2), as shown in Fig. 4. In our simulations, we use $\beta = 25$, and the total pulse duration $\tau = n(2\pi/\omega)$ is set as $n = 2$ laser cycles, and it approximately equals 4 fs. It is worth noting that, in the last decade, ultrashort laser pulses with the aforementioned characteristics have become largely available to experimentalists in the attosecond physics community. In fact, the laser pulse we use in our simulations is essentially the one commonly used for the attoclock scheme [104–106].

Moreover, since the entanglement between the parent ion and the photoelectron is encoded in the spin degree of freedom of the latter, and not in its kinetic energy, the time duration of the photoionizing pulse is not a sensitive parameter for the formation of this type of entanglement. A short duration of the photoionizing pulse will result in an overlap in kinetic energy of the photoelectron wave packets coming out of the ground-state spin-orbit doublet of the parent ion. In contrast, a pulse with longer duration would give rise to two series of above-threshold-ionization (ATI) peaks in the photoelectron spectrum, one shifted with respect to the other by the difference between the ionization

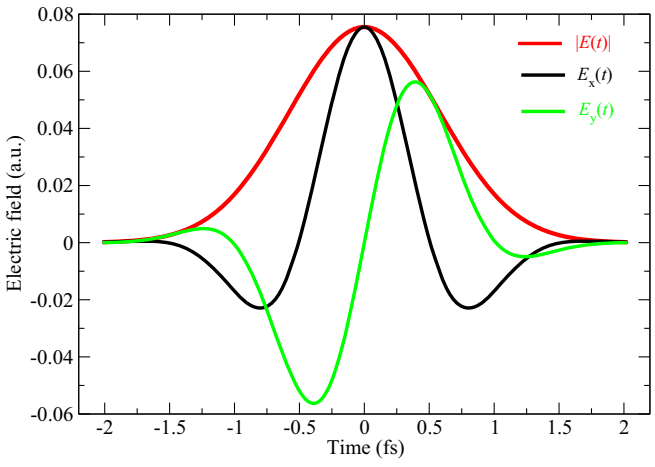


FIG. 4. Time dependence of the electric-field components in the $x - y$ plane of the circularly polarized pulse used in this work. The absolute value of the electric-field vector is also shown.

potential of the ground and first excited states of the argon cation. These two different scenarios should result in difference levels of entanglement (low and high, respectively) encoded in the photoelectron's kinetic energy, but we do not expect the entanglement encoded in the spin degree of freedom to be significantly affected.

B. Results and discussion

In Fig. 5, we show the angle-integrated kinetic-energy-dependent matrix elements of the density matrix $\hat{\tilde{\rho}}^{\xi}$ in Eq. (B1) resulting from photoionization of an argon atom by the laser pulse described in the previous subsection. The density matrix is normalized at each value of the photoelectron's kinetic energy. The diagonal matrix elements $\tilde{\rho}^{\xi}_{i,i} = P_i$ correspond to the populations P_i of the six states in Eq. (2) and Figs. 1 and 3. As can be seen in Fig. 5(a), our *ab initio* numerical results confirm, over the majority of the kinetic-energy range, and quantify the predominance of ionization from the states $|^2P_{1/2,+1/2};\uparrow\rangle$ and $|^2P_{3/2,+3/2};\downarrow\rangle$, here labeled states 1 and 2, respectively, which reflects the preferred emission of counterrotating p_{-1} electrons, as also predicted with elegant analytical techniques (yet applied to a more approximate model of the argon atom) in Ref. [83]. The off-diagonal matrix elements shown in Fig. 5 are the ones that contribute to the Bell inequality [see Eq. (B21)]: In the lower left panel, we show the real and imaginary parts of the angle-integrated, kinetic-energy-dependent density matrix elements $\tilde{\rho}^{\xi}_{21}$, $\tilde{\rho}^{\xi}_{51}$, and $\tilde{\rho}^{\xi}_{52}$ between the states $|^2P_{1/2,+1/2};\uparrow\rangle$ (1), $|^2P_{3/2,+3/2};\downarrow\rangle$ (2), and $|^2P_{3/2,-1/2};\downarrow\rangle$ (5) that are coupled to each other by the ionic pulse scheme (see Fig. 3). In the lower right panel, we show the real and imaginary parts of the angle-integrated, kinetic-energy-dependent density matrix elements $\tilde{\rho}^{\xi}_{43}$, $\tilde{\rho}^{\xi}_{63}$, and $\tilde{\rho}^{\xi}_{64}$ between the other set of states $|^2P_{1/2,-1/2};\downarrow\rangle$ (4), $|^2P_{3/2,+1/2};\uparrow\rangle$ (3), and $|^2P_{3/2,-3/2};\uparrow\rangle$ (6) that are also coupled to each other by the ionic pulse scheme (see Fig. 3). The results of Fig. 5 show that the phases of the complex off-diagonal elements of the density matrix have a nontrivial dependence on the photoelectron energy, and that most pairs of states are characterized by a high degree of coherence across a wide kinetic-energy range (the squared absolute value of their off-diagonal matrix element is close to the product of their corresponding populations $|\tilde{\rho}^{\xi}_{ij}|^2 \approx P_i \times P_j$).

In Fig. 6, we show the energy-dependent photoelectron angular distribution (PAD) and the values of the Bell function $\mathbb{S}$ from Eq. (6) obtained by postselecting photoionization events characterized both by specific values of the photoelectron's kinetic energy and of its emission angle Φ in the polarization plane of the photoionizing laser pulse. Values of $\mathbb{S}$ greater than 2 correspond to a violation of the Bell inequality and a direct detection of entanglement. The results show that postselecting events where not only

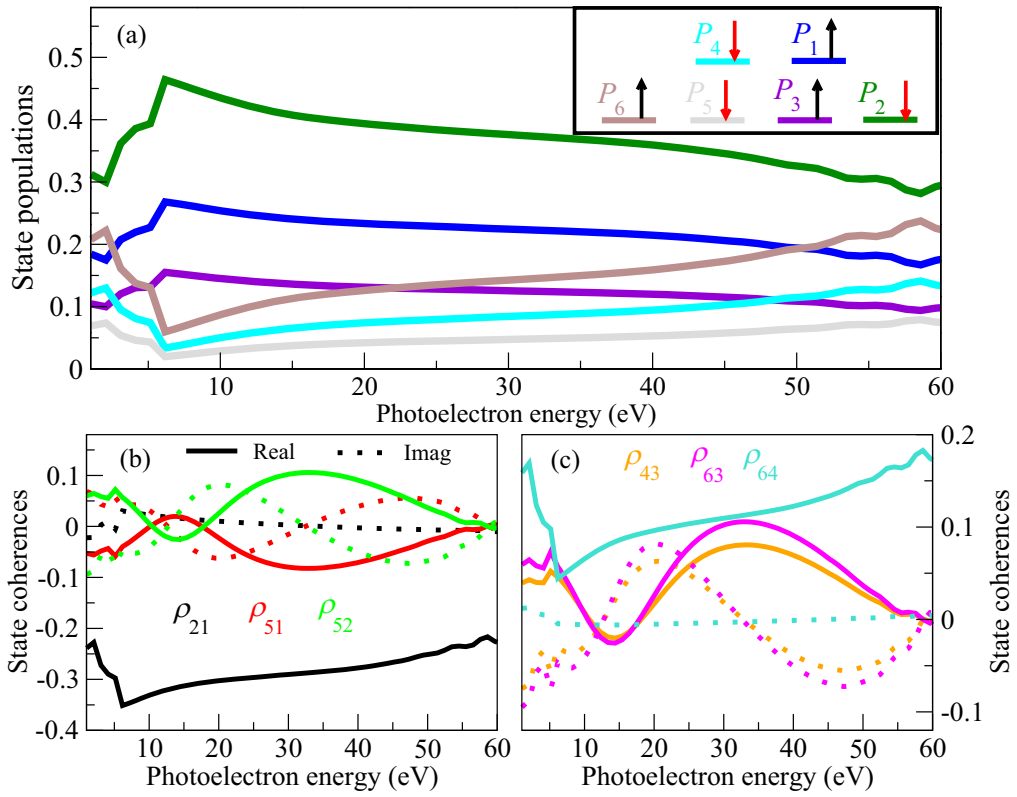


FIG. 5. (a) Normalized, angle-integrated, kinetic-energy-dependent diagonal elements of the effective density matrix $\tilde{\rho}^{\xi}_{i,i}$ in Eq. (A7) upon photoionization of Ar by a circularly polarized two-cycle laser pulse with peak intensity $I_{\text{peak}} = 2 \times 10^{14}$ W/cm^2 and $\hbar\omega_{\text{central}} = 2$ eV central photon energy. The diagonal matrix elements $\tilde{\rho}^{\xi}_{i,i} = P_i$ correspond to the populations P_i of the six states in Eq. (2) and Figs. 1 and 3. (b) Normalized, angle-integrated, kinetic-energy-dependent $\tilde{\rho}^{\xi}_{21}$, $\tilde{\rho}^{\xi}_{51}$, and $\tilde{\rho}^{\xi}_{52}$ off-diagonal element of the effective density matrix [see Eq. (A8)] between the states $|^2P_{1/2,+1/2};\uparrow\rangle$ (1), $|^2P_{3/2,+3/2};\downarrow\rangle$ (2), and $|^2P_{3/2,-1/2};\downarrow\rangle$ (5), which are coupled to each other by the ionic pulse scheme (see Fig. 3). (c) Normalized, angle-integrated, kinetic-energy-dependent $\tilde{\rho}^{\xi}_{43}$, $\tilde{\rho}^{\xi}_{63}$, and $\tilde{\rho}^{\xi}_{64}$ off-diagonal element of the effective density matrix [see Eq. (A8)] between the states $|^2P_{1/2,-1/2};\downarrow\rangle$ (4), $|^2P_{3/2,+1/2};\uparrow\rangle$ (3), and $|^2P_{3/2,-3/2};\uparrow\rangle$ (6), which are coupled to each other by the ionic pulse scheme (see Fig. 3).

the emission occurs in specific spatial directions, but also the photoelectron has specific kinetic energy, gives rise to a strong violation of the resulting Bell inequalities, the value of $\mathbb{S}$ reaching approximately 2.44.

The photoelectron emission is mostly focused in the angular region in the vicinity of the x axis, i.e., in the $[-5°–75°]$ angular range. This is due to the ultrashort duration of the photoionizing laser pulse, whose electric-field amplitude is strongly peaked at a time where the electric-field vector lies of the positive side of the x axis (see Fig. 4). Note that this type of photoionization regime is essentially the one commonly used to perform attosecond angular streaking and photoionization time-delay measurements based on the attoclock principle [104–106]. In particular, the PAD is peaked at $\Phi_{\text{max}} = 26°$ and $\xi_{\text{max}} = 36$ eV, where we can observe both a strong photoelectron signal and a robust violation of the Bell inequality given by $\mathbb{S} \approx 2.37$. Persistent violation of the Bell inequality can be observed over a wide area that also corresponds to the region where the photoelectron emission is mostly concentrated. The laser parameters $((\Omega_b/\Omega_a), \Omega_{\text{eff}} \times T, \phi)$ that determine the ionic operators $\hat{Q}^{\text{Ion}}$ and $\hat{R}^{\text{Ion}}$ have been optimized for each postselection choice in order to maximize the violation of the resulting Bell inequality. The optimal ionic operators that allow one to maximize the violation of the corresponding Bell inequality are characterized as follows: In the case of the operator $\hat{Q}$, the ratio between the Rabi frequencies of the two applied resonant pulses is given by $(\Omega_b/\Omega_a)_{\hat{Q}} \sim 1.1$, the duration of the laser pulses needs to satisfy $(\Omega_{\text{eff}} \times T)_{\hat{Q}} \sim \pi + 2N\pi (N = 0, 1, 2, \ldots)$, and the phase difference between the two electric fields is $\phi_{\hat{Q}} \sim (3\pi/2) \pm 2N\pi (N = 0, 1, 2, \ldots)$. In the case of the operator $\hat{R}$, the ratio between the Rabi frequencies of the two applied resonant pulses is given by $(\Omega_b/\Omega_a)_{\hat{R}} \sim 2.1$, the duration of the laser pulses needs to satisfy $(\Omega_{\text{eff}} \times T)_{\hat{R}} \sim \pi + 2N\pi (N = 0, 1, 2, \ldots)$, and the phase difference between the two electric fields is also $\phi_{\hat{R}} \sim (3\pi/2) \pm 2N\pi (N = 0, 1, 2, \ldots)$.

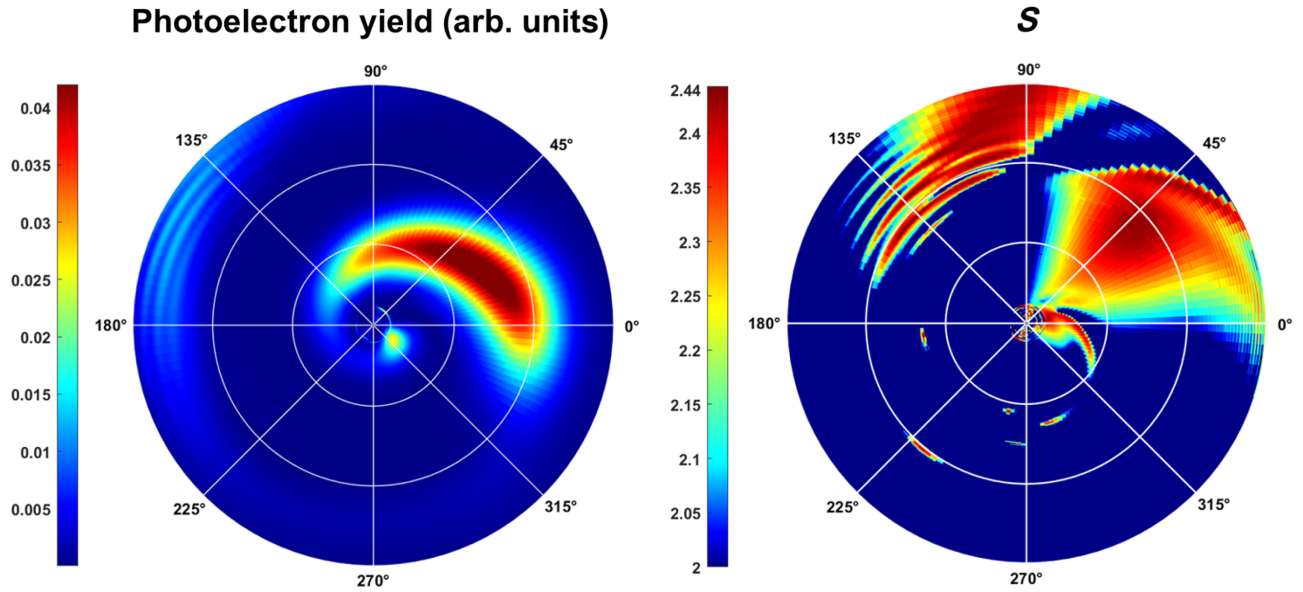


FIG. 6. Left plot: Φ angle (in the polarization plane of the photoionizing field) and kinetic-energy-dependent photoelectron yield upon photoionization of Ar by a circularly polarized two-cycle laser pulse with peak intensity $I_{\text{peak}} = 2 \times 10^{14}$ W/cm^2 and $\hbar\omega_{\text{central}} = 2$ eV central photon energy. The radial coordinate indicates the kinetic energy of the photoelectron; the interval between neighboring concentric circles is 24 eV. Right plot: Φ angle (in the polarization plane of the photoionizing field) and optimized kinetic-energy-dependent value of the Bell inequality quantity $\mathbb{S}$ from Eq. (6). Values greater than 2 correspond to a violation of the Bell inequality.

In Fig. 7, we show the calculated photoelectron yield and the calculated expectation value of the operator $\mathbb{S}$ that defines the Bell inequality in Eq. (6) as a function of the photoelectron's kinetic energy. This case would correspond to the experimental protocol characterized by postselection of photoionization events characterized by a value of the photoelectron's kinetic energy in specific ranges. Here, it is worth mentioning that the range of values over which performing the postselection is limited only by the resolution of the photoelectron spectrometer and/or by the minimum or maximum kinetic energy that is detectable. The results of Fig. 7 show that the broad photoelectron yield extends over a wide range of kinetic energies, with a broad peak between 20 and 35 eV and a maximum around 26 eV. The broadness of the energy-dependent photoelectron spectrum, which lacks the typical ATI peak structure, is due to the short duration of the laser pulse we used in this work. The calculated channel-resolved spin polarizations reach the values 80% and −40% for the $^2P_{1/2}$ and $^2P_{3/2}$ channels, respectively. The laser parameters $((\Omega_b/\Omega_a), \Omega_{\text{eff}} \times T, \phi)$ that determine the ionic operators $\hat{Q}^{\text{Ion}}$ and $\hat{R}^{\text{Ion}}$ have been optimized for each postselection choice in order to maximize the violation of the resulting Bell inequality. Violation of the Bell inequality can be observed over a wide range of photoelectron kinetic energies. The maximum violation with $\mathbb{S} \approx 2.26$ can be observed for events where the detected photoelectron has a kinetic energy around 28–30 eV. The ionic operators that construct, and maximize the violation of, the corresponding Bell inequality are characterized as follows: In the case of the $\hat{Q}$ operator, the ratio between the Rabi frequencies of the two applied resonant pulses is given by $(\Omega_b/\Omega_a)_{\hat{Q}} \sim 1.1$, the duration of the laser pulses needs to satisfy $(\Omega_{\text{eff}} \times T)_{\hat{Q}} \sim \pi + 2N\pi (N = 0, 1, 2, \ldots)$, and the phase difference between the two electric fields is $\phi_{\hat{Q}} \sim (3\pi/2) \pm 2N\pi (N = 0, 1, 2, \ldots)$. In the case of the $\hat{R}$ operator, the ratio between the Rabi frequencies of the two applied resonant pulses is given by $(\Omega_b/\Omega_a)_{\hat{R}} \sim 2.1$, the duration of the laser pulses needs to satisfy $(\Omega_{\text{eff}} \times T)_{\hat{R}} \sim \pi + 2N\pi (N = 0, 1, 2, \ldots)$, and the phase difference between the two electric fields also is $\phi_{\hat{R}} \sim (3\pi/2) \pm 2N\pi (N = 0, 1, 2, \ldots)$. Note that these values are essentially the same that maximize the violation of the energy- and angle-dependent Bell inequality; i.e., the values of the control pulse parameters to be used for this Bell test when photoionization events are postselected over the measured value of the full photoelectron momentum also give maximum violation in the postselection of the photoelectron's kinetic energy only.

In Fig. 8, we show the kinetic-energy-integrated photoelectron yield, the channel-resolved spin polarization for the $J = 1/2$ and the $J = 3/2$ ionization channels, and the values of the Bell function $\mathbb{S}$ from Eq. (6) obtained by postselecting photoionization events characterized only by specific values of the photoelectron's emission angle Φ in the polarization plane of the photoionizing laser pulse. The calculated channel-resolved spin polarizations reach the values 60% and −35% for the $^2P_{1/2}$ and $^2P_{3/2}$ channels, respectively. The results of Fig. 8 show that a robust violation of the Bell inequality can be observed over the

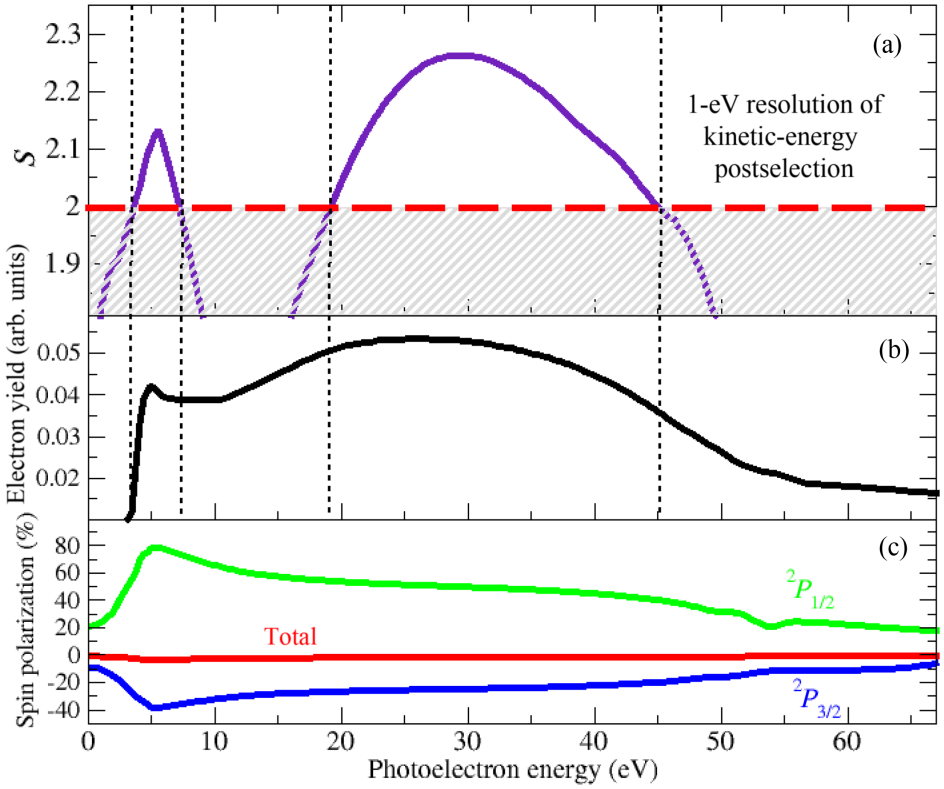


FIG. 7. (a) Value of the Bell inequality quantity $\mathbb{S}$ from Eq. (6) optimized as a function of the postselected value of the photoelectron's kinetic energy. Values greater than 2 correspond to a violation of the Bell inequality. (b) Angle-integrated, kinetic-energy-dependent photoelectron yield upon photoionization of Ar by a circularly polarized, two-cycle laser pulse with peak intensity $I_{\text{peak}} = 2 \times 10^{14}$ W/cm^2 and $\hbar\omega_{\text{central}} = 2$ eV central photon energy. (c) Dependence of the spin polarization, both channel resolved [$\text{Pol}_S^{^2P_{3/2}}$ and $\text{Pol}_S^{^2P_{1/2}}$; see Eq. (3)] and total, on the photoelectron's kinetic energy.

range of angles $[-15°, 75°]$ around the x axis, where 80% of the total electron yield is also found. The maximum violation with $\mathbb{S} \approx 2.39$ can be observed for events where the detected emission angle of the photoelectron in the laser polarization plane is around 30°. These results show that disregarding the kinetic energy of the photoelectron and postselecting events where emission happens in specific spatial directions can give rise to stronger violation of the resulting Bell inequalities with respect to the previously presented case of postselection over the value of the photoelectron's kinetic energy. Again, the laser parameters $((\Omega_b/\Omega_a), \Omega_{\text{eff}} \times T, \phi)$ that determine the ionic operators $\hat{Q}^{\text{Ion}}$ and $\hat{R}^{\text{Ion}}$ have been optimized in order to maximize the violation of the resulting Bell inequality. The ionic operators that construct, and maximize the violation of, the corresponding Bell inequality are characterized as follows: In the case of the operator $\hat{Q}$, the ratio between the Rabi frequencies of the two applied resonant pulses is given by $(\Omega_b/\Omega_a)_{\hat{Q}} \sim 1.0$, the duration of the laser pulses needs to satisfy $(\Omega_{\text{eff}} \times T)_{\hat{Q}} \sim \pi + 2N\pi (N = 0, 1, 2, \ldots)$, and the phase difference between the two electric fields is $\phi_{\hat{Q}} \sim (3\pi/2) \pm 2N\pi (N = 0, 1, 2, \ldots)$. In the case of the operator $\hat{R}$, the ratio between the Rabi frequencies of the two applied resonant pulses is given by $(\Omega_b/\Omega_a)_{\hat{R}} \sim 2.0$, the duration of the laser pulses needs to satisfy $(\Omega_{\text{eff}} \times T)_{\hat{R}} \sim \pi + 2N\pi (N = 0, 1, 2, \ldots)$, and the phase difference between the two electric fields is also $\phi_{\hat{R}} \sim (3\pi/2) \pm 2N\pi (N = 0, 1, 2, \ldots)$. Note that also these values are very similar to the ones that maximize the violation of the energy- and angle-dependent Bell inequality; i.e., the values of the control pulse parameters that maximize the Bell inequality's violation when photoionization events are postselected over the measured value of the full photoelectron momentum also give strong violation in the case of postselection over the photoelectron's emission direction only.

Therefore, in the photoionization regime described in this work, the optimal laser parameters that need to be chosen to perform the measurements on the parent ion and maximize the entanglement detection have a negligible dependence on the type of postselection, i.e., on whether or not the linear momentum of the photoelectron is also fully detected, in addition to its spin angular momentum.

C. Estimation of the experimental feasibility

The Bell test we propose to directly probe the entanglement between a photoelectron and the ion upon an ultrafast

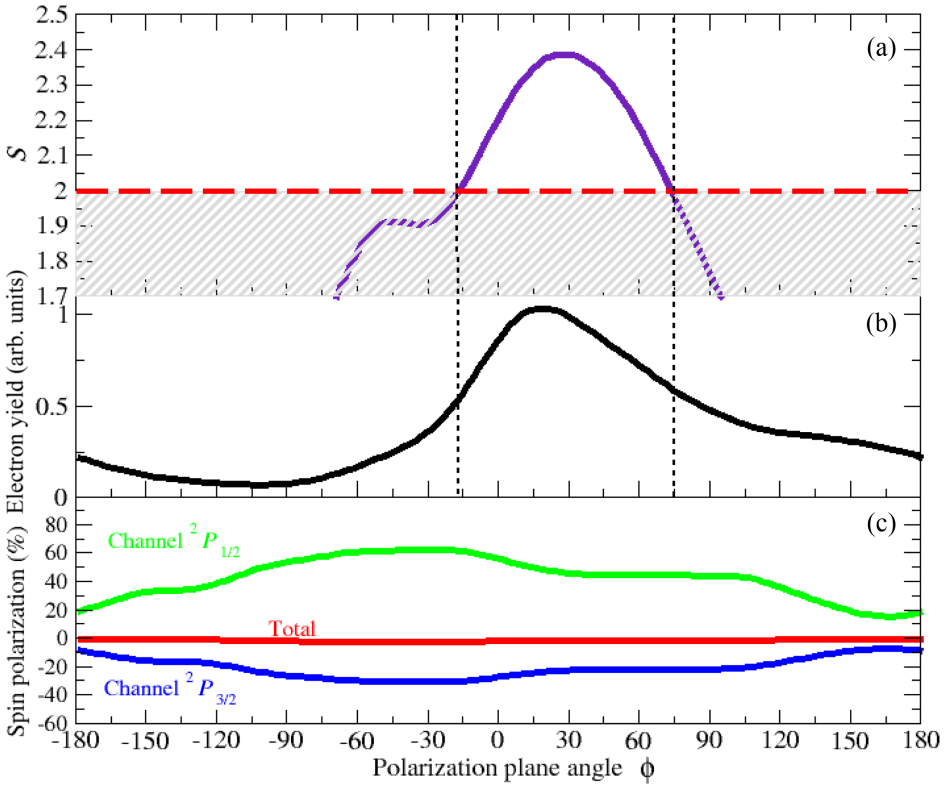


FIG. 8. (a) Value of the Bell inequality quantity $\mathbb{S}$ from Eq. (6) optimized as a function of the postselected value of the photoelectron angle of emission in the polarization plane of the photoionizing field. Values greater than 2 correspond to a violation of the Bell inequality. (b) Kinetic-energy-integrated, angle-of-emission-dependent photoelectron yield upon photoionization of Ar by a circularly polarized, two-cycle laser pulse with peak intensity $I_{\text{peak}} = 2 \times 10^{14}$ W/cm^2 and $\hbar\omega_{\text{central}} = 2$ eV central photon energy. (c) Dependence of the spin polarization, both channel resolved [$\text{Pol}_S^{^2P_{3/2}}$ and $\text{Pol}_S^{^2P_{1/2}}$; see Eq. (3)] and total, on the photoelectron angle of emission in the polarization plane of the photoionizing field.

photoionization process involves measurement of the photon fluorescence from the parent ion in coincidence with the detection of the photoelectron.

The most essential experimental parameters that are needed to estimate the time duration of such a coincidence experiment are the detection probabilities P_i of the respective particles i = photon, electron, the repetition rate of the photoionizing laser, and the number of photoionization events per laser pulse. In the following, we will discuss realistic values for the key parameters, comment on the needed and available experimental techniques, and provide an estimate of the expected time duration of the proposed experiment.

The photon and electron detection probabilities P_i can be separated into products of the corresponding accepted relative solid angles $\Sigma_{\text{rel},i} (\in [0, 1])$ and detector efficiencies $\epsilon_i (\in [0, 1])$. The detector efficiency ϵ_i is the probability that a particle reaching the detector is recorded as an actual event, and it is an intrinsic characteristic of the detector. However, the achievable solid angle is given by the experimental geometry. In general, it can be described by the active detector surface area A_D and its distance to the interaction volume D, $\Sigma_{\text{rel}} \approx (A_D/4\pi D^2)$.

In the case of photoelectrons, the accepted relative solid angle $\Sigma_{\text{rel,electron}}$ can often be increased to values close to unity by guiding the charged particles toward the active detector area via electric and/or magnetic fields. Prominent examples for the latter case are "reaction microscope" experiments in which charged fragments of atoms, molecules, or clusters are measured in multiple coincidences. Here it is interesting to note that, in the photoionization process described in this work, the photoemission is mostly concentrated in a relatively small solid angle along the direction of the electric-field's peak. Therefore, placing the active photoelectron detector in the optimal direction relative to the propagation direction of the photoionizing laser already allows one to reach large values of the accepted relative solid angle. The overall efficiency of the coincidence detection will also depend on the efficiency of the method used for measuring the photoelectron spin. As already mentioned, the spin detection efficiency that can be achieved with a Mott polarimeter is $\epsilon_{\text{electron}} \approx 2 \times 10^{-4}$. However, more efficient spin detection techniques can be used. For example, electron spin detection based on spin-exchange interaction and energy-exchange scattering from Fe (001)

epitaxial films can give efficiencies as high as $\epsilon_{\text{electron}} \approx 3.3 \times 10^{-2}$ [77,78].

As far as photon detection is concerned, the feasibility of such detection in coincidence with photoelectrons has been repeatedly demonstrated over the years [107–110]. Efficient electron-photon coincidence setups are characterized by an optics that allows one to increase the solid angle for photon detection up to $\Sigma_{\text{rel,photon}} \approx 0.4$ [107]. Photons are detected undispersedly (or with a wavelength bandpass filter) and in coincidence with photoelectrons. In particular, the setup described in Ref. [107] was successfully used in experiments based on electron-photon coincidence, which demonstrated radiative charge transfer [108] and core-level interatomic Coulombic decay in clusters [109]. Moreover, recently even triple electron-electron-photon coincidence spectroscopy was successfully used to experimentally observe Auger decay in the field of a positive elementary charge [110]. In these works [108–110], the measurement of electron-photon coincidence was instrumental in disentangling an electron signal and a photon signal from a large background originating from other processes. In addition, this kind of setup [107] enables photon detection with high temporal resolution (approximately equal to 35 ps) works without transmissive optics and is therefore suitable for the detection of photons in the vacuum ultraviolet to soft x-ray wavelength regime.

As far as the photoionization process is concerned, the repetition rate of the photoionizing laser can be assumed [111,112] to be $\alpha \times 50$ KHz, where the parameter α varies between 0.02 and 4.0 [112]. In addition, to effectively reduce the detection of false coincidences, it is reasonable to operate within an experimental setting where a maximum of 0.1 ionization events per laser pulse is possible. Finally, within these parameter settings, we obtain a number of photoionization events detected per second $N_{\text{detected}} \approx 0.66 \times \alpha \times 10^2$ events/s. In order to give an estimate of the time duration of the proposed experiment, we can assume a total of at least 4×10^5 events to be detected [approximately 10^5 events per each of the terms composing the quantity $\mathbb{S}$; see Eq. (6)], which is in line with the coincidence statistics typical for Bell test experiments [113–115]. This results in an experiment time $T_{\text{Expt}} \approx 0.6 \times (10^2/\alpha)$ s, which ranges from approximately 25 minutes for $\alpha = 4$ (200-KHz repetition rate [112]), to approximately 79 hours in the case $\alpha = 0.02$ (1-KHz repetition rate), which are reasonable data acquisition times for a coincidence experiment.

In addition, even by using a photoionizing laser's repetition rate as high as 50 KHz, a maximum of 0.1 ionization events per laser pulse gives a number of photoionization events per second equal to 5×10^3 events/s. Consequently, the time between subsequent photoionizing events is at least 0.02 ms. This is certainly enough time to perform both the laser ionic manipulation and to detect the fluorescence emission from the second excited state $^2S_{1/2}$ of the Ar^+ cation, whose lifetime is approximately 7 ns [116].

In fact, the time duration of the ionic manipulation pulses can be written as

$$\frac{\Omega_b}{\Omega_a} = \sqrt{3} \times \frac{E_{\text{y}}^{(2)}}{E_{\text{z}}^{(1)}}, \quad T = \frac{\pi}{d_A \sqrt{\left(E_{\text{z}}^{(1)}\right)^2 + 2\left(E_{\text{y}}^{(2)}\right)^2}}, \tag{10}$$

where the Rabi frequencies of Fig. 3 are given by $\Omega_a = E_{\text{z}}^{(1)} d_A$ and $\Omega_b = E_{\text{y}}^{(2)} d_B$, and the values of the transition dipoles are $d_A = 0.498$ a.u. and $d_B = \sqrt{3} \times d_A = 0.8624$ a.u. Therefore, using the optimal parameters derived in Sec. III B for the case of postselection over the photoelectron emission direction, we have for the case of the $\hat{Q}^{\text{Ion}}$ operator ($(\Omega_b/\Omega_a) \sim 1.0$),

$$E_{\text{z}}^{(1)} = \sqrt{3} \times E_{\text{y}}^{(2)}, \qquad T = \frac{\pi}{d_A E_{\text{y}}^{(2)} \sqrt{5}} = \frac{2.82}{E_{\text{y}}^{(2)}} \text{ a.u.}, \tag{11}$$

and for the case of the $\hat{R}^{\text{Ion}}$ operator ($(\Omega_b/\Omega_a) \sim 2.0$),

$$E_{\text{z}}^{(1)} = \frac{\sqrt{3}}{2} \times E_{\text{y}}^{(2)}, \quad T = \frac{2\pi}{d_A E_{\text{y}}^{(2)} \sqrt{11}} = \frac{3.8}{E_{\text{y}}^{(2)}} \text{ a.u.} \tag{12}$$

Using electric-field strengths on the order of 5×10^{-4} a.u. (intensities on the order of 10^{10} W/cm^2), we obtain corresponding time durations on the order of a few hundred femtoseconds.

The required photon energy can be obtained using a high-harmonic pulse: Table-top, compact setups based on HHG can indeed be used to generate intense, narrow-band extreme-ultraviolet pulses dominated by a single harmonic order [117]. Femtosecond extreme-ultraviolet pulses with narrow spectral bandwidth can also be generated by a seeded free-electron-laser (FEL) source, such as the FERMI FEL that delivers radiation in the range of (12–120)-eV photon energy, and where Rabi dynamics between the ground state and an excited state in helium atoms has been recently studied using such pulses [118].

To conclude, our proposed Bell test presents a set of key experimental requirements, that is, (i) atomic photoionization by intense, circularly polarized IR pulses, (ii) the use of a pair of delayed control pulses (e.g., high-harmonic pulses), (iii) photoelectron spin detection, and (iv) coincidence detection of the photoelectron with the photon emitted by the cation. While all the key experimental technologies required for such an experiment have been demonstrated in several different experiments, an experimental realization of the proposed Bell test would need to be conceptualized to include all these individually realized aspects. Important progress has already been made in the direction of integrating the aforementioned requirements

into a single experiment; e.g., in Refs. [73,74], photoelectron spin detection (using a Mott polarimeter) was combined with photoionization of atomic gases by intense circularly polarized IR laser pulses. Moreover, in Ref. [82] the capability of integrating highly efficient LEED spin detection, both with time-resolved measurements involving pump-and-probe-delayed laser pulses, and with angle-resolved photoemission spectroscopy, has been demonstrated. In particular, the equipment of Ref. [82] effectively combines the technologies of a high-power pump-laser system at the high repetition rate of 1 MHz, a delayed single-harmonic probe pulse generated by ultraviolet-driven harmonic generation in Xe gas, and a spin-ARPES apparatus equipped with LEED spin detectors.

IV. CONCLUSION AND OUTLOOK

The results presented here predict that strong violation of Bell inequalities can be observed in ultrafast photoionization experiments. This challenges the appropriateness of treating the photoelectron and the ion as individual systems and highlights the experimental relevance of electron-ion correlations.

The present work paves the way to the direct observation of entanglement in the context of ultrafast photoionization of many-electron systems, the latter not being restricted to the case of strong-field ionization of atomic systems. In fact, other photoionization regimes can feature in the spin polarization of the photoelectron beam such as, for example, single-photon ionization, either from a particular fine-structure level of an atom or a molecule [87] or in the vicinity of the Cooper minima in the photoionization continua [88], and resonant multiphoton ionization in the perturbative limit [89,90]. Moreover, it is worth noting that the detection of entanglement in attosecond photoionization is not necessarily limited to the measurement of the spin degree of freedom of the photoelectron, but can in general also be extended to Bell tests based on the observation of the photoelectron's orbital angular momentum that is already becoming experimentally accessible [70–72].

Our work opens up a novel perspective on attosecond physics directed toward the development of new types of spectroscopy targeted to detect the different types of quantum correlation present in attoionized states of quantum systems. A key step forward for future work on the subject consists of extending this type of protocol to molecular systems and, in particular, investigating the quantum correlations that can exist between the state of the photoelectron and the outcome of a chemical reaction pathway in the parent, excited molecular ion, with the ultimate goal of giving an answer to the following research question: What is the dependence of the observed hole migration dynamics in the molecular ion on the detection scheme of the entangled state created by photoionization?

Finally, our work also opens up the possibility to coherently control entanglement in photoionized systems by performing photoionizing pulse shaping with the aim of detecting specific quantum correlations in coincidence measurements.

ACKNOWLEDGMENTS

The authors acknowledge support from the EPSRC grant "Quantum entanglement in attosecond ionization," Grant No. EP/V009192/1. The authors would like to thank M. Drescher, R. Dörner, and A. Ehresmann for fruitful discussions.

APPENDIX A: EFFECTIVE REDUCED DENSITY MATRIX

The final state of the photoionized atom can be written as

$$|\Psi_N^F\rangle = \sum_j \sum_{\mathbf{s}} \iint d\xi d\alpha C_j(\xi,\mathbf{s},\alpha)|j;\xi,\mathbf{s},\alpha\rangle, \tag{A1a}$$

$$|j;\xi,\mathbf{s},\alpha\rangle = |I_j^+\rangle \otimes |e^-_{\xi,\mathbf{s},\alpha}\rangle. \tag{A1b}$$

In Eqs. (A1), the index j labels the different internal bound states of the parent ion, ξ is the kinetic energy of the photoelectron, $\mathbf{s}$ its spin component along a specific axis in space (in the present case, the propagation direction of the photoionizing laser beam), and α denotes any extra continuous degree of freedom describing the state of the photoelectron, e.g., the emission angles.

The density matrix of the full composite system can be written as

$$\rho_{i\xi\alpha\mathbf{s},j\xi'\alpha'\mathbf{s}'} = C_i(\xi,\mathbf{s},\alpha) \times C_j^*(\xi',\mathbf{s}',\alpha'). \tag{A2}$$

Within a specific measurement protocol, it is possible to either ignore (i.e., do not measure) some of the observables characterizing a particular subsystem or to use these observables to postselect the events in which only some specific outcomes of their measurement are observed. The former scenario is equivalent to considering an effective reduced density matrix, which can be obtained from Eqs. (A2) by tracing over the unobserved degree of freedom, for example, in the case of α,

$$\hat{\tilde{\rho}} = \mathrm{Tr}_\alpha(\hat{\rho}), \tag{A3}$$

$$\tilde{\rho}_{i\xi\mathbf{s},j\xi'\mathbf{s}'} = \int d\alpha C_i(\xi,\mathbf{s},\alpha) \times C_j^*(\xi',\mathbf{s}',\alpha). \tag{A4}$$

Postselection over the value of the photoelectron's kinetic energy gives rise to a final effective density matrix parametrized with respect to ξ:

$$\tilde{\rho}^{\xi}_{i\mathbf{s},j\mathbf{s}'} = \int d\alpha C_i(\xi,\mathbf{s},\alpha) \times C_j^*(\xi,\mathbf{s}',\alpha). \tag{A5}$$

In the case where the degree of freedom α consists of the direction of emission of the photoelectron, as can be measured in a photoelectron angular distribution experiment, we have for example,

$$\tilde{\rho}^{\xi}_{i\uparrow,j\downarrow} = \int C_{i,\uparrow}(\xi,\theta,\Phi) \times C^{*}_{j,\downarrow}(\xi,\theta,\Phi)\sin(\theta)d\theta d\Phi. \quad \text{(A6)}$$

The diagonal elements of this effective density matrix are given by

$$\tilde{\rho}^{\xi}_{i\mathbf{s},i\mathbf{s}} = \int d\alpha |C_i(\xi,\mathbf{s},\alpha)|^2 = |\tilde{C}_i(\xi,\mathbf{s})|^2. \quad \text{(A7)}$$

Here it is important to note that the off-diagonal matrix elements $\tilde{\rho}^{\xi}_{i\mathbf{s},j\mathbf{s}'}$ cannot be in general simplified by the real-valued product $|\tilde{C}_i(\xi,\mathbf{s})| \times |\tilde{C}_j(\xi,\mathbf{s}')|$, rather they read as

$$\tilde{\rho}^{\xi}_{i\mathbf{s},j\mathbf{s}'} = |\tilde{C}_i(\xi,\mathbf{s})||\tilde{C}_j(\xi,\mathbf{s}')|G_{i\mathbf{s},j\mathbf{s}'}(\xi) \times e^{i\tilde{\chi}^{\xi}_{i\mathbf{s},j\mathbf{s}'}}. \quad \text{(A8)}$$

In Eq. (A8),

$$G_{i\mathbf{s},j\mathbf{s}'}(\xi) = \frac{|\tilde{\rho}^{\xi}_{i\mathbf{s},j\mathbf{s}'}|}{\sqrt{\tilde{\rho}^{\xi}_{i\mathbf{s},i\mathbf{s}} \times \tilde{\rho}^{\xi}_{j\mathbf{s}',j\mathbf{s}'}}}$$

is the energy-dependent degree of coherence between the i, $\mathbf{s}$ and the $j,\mathbf{s}'$ states of the composite parent ion and photoelectron system.

APPENDIX B: DERIVATION OF THE BELL INEQUALITY FOR THE IONIC MEASUREMENT SCHEME

The pulse scheme introduced in Sec. II involves all the ionic states populated by the photoionizing laser pulse. The effective density matrix of the Ar^+ parent ion produced by the photoionization process, and structured according to two blocks each containing the states coupled by the synchronized laser pulses applied to the cation, reads as

$$\tilde{\rho}^{\xi} = \begin{pmatrix} |\tilde{C}_{1,\uparrow}(\xi)|^2 & \tilde{\rho}_{1\uparrow,2\downarrow}(\xi) & \tilde{\rho}_{1\uparrow,5\downarrow}(\xi) & \tilde{\rho}_{1\uparrow,3\uparrow}(\xi) & \tilde{\rho}_{1\uparrow,4\downarrow}(\xi) & \tilde{\rho}_{1\uparrow,6\uparrow}(\xi) \\ \tilde{\rho}^{*}_{1\uparrow,2\downarrow}(\xi) & |\tilde{C}_{2,\downarrow}(\xi)|^2 & \tilde{\rho}_{2\downarrow,5\downarrow}(\xi) & \tilde{\rho}_{2\downarrow,3\uparrow}(\xi) & \tilde{\rho}_{2\downarrow,4\downarrow}(\xi) & \tilde{\rho}_{2\downarrow,6\uparrow}(\xi) \\ \tilde{\rho}^{*}_{1\uparrow,5\downarrow}(\xi) & \tilde{\rho}^{*}_{2\downarrow,5\downarrow}(\xi) & |\tilde{C}_{5,\downarrow}(\xi)|^2 & \tilde{\rho}_{5\downarrow,3\uparrow}(\xi) & \tilde{\rho}_{5\downarrow,4\downarrow}(\xi) & \tilde{\rho}_{5\downarrow,6\uparrow}(\xi) \\ \tilde{\rho}^{*}_{1\uparrow,3\uparrow}(\xi) & \tilde{\rho}^{*}_{2\downarrow,3\uparrow}(\xi) & \tilde{\rho}^{*}_{5\downarrow,3\uparrow}(\xi) & |\tilde{C}_{3,\uparrow}(\xi)|^2 & \tilde{\rho}_{3\uparrow,4\downarrow}(\xi) & \tilde{\rho}_{3\uparrow,6\uparrow}(\xi) \\ \tilde{\rho}^{*}_{1\uparrow,4\downarrow}(\xi) & \tilde{\rho}^{*}_{2\downarrow,4\downarrow}(\xi) & \tilde{\rho}^{*}_{5\downarrow,4\downarrow}(\xi) & \tilde{\rho}^{*}_{3\uparrow,4\downarrow}(\xi) & |\tilde{C}_{4,\downarrow}(\xi)|^2 & \tilde{\rho}_{4\downarrow,6\uparrow}(\xi) \\ \tilde{\rho}^{*}_{1\uparrow,6\uparrow}(\xi) & \tilde{\rho}^{*}_{2\downarrow,6\uparrow}(\xi) & \tilde{\rho}^{*}_{5\downarrow,6\uparrow}(\xi) & \tilde{\rho}^{*}_{3\uparrow,6\uparrow}(\xi) & \tilde{\rho}^{*}_{4\downarrow,6\uparrow}(\xi) & |\tilde{C}_{6,\uparrow}(\xi)|^2 \end{pmatrix}. \quad \text{(B1)}$$

The $|^2S\rangle$ bound excited state is not populated by the photoionization process, and it has therefore been omitted in Eq. (B1).

The measurement protocol on the parent ion subsystem consists of

(i) Application of the two collinear, control laser pulses linearly polarized along two perpendicular directions as described in Figs. 2 and 3.

(ii) Detection of fluorescence emission from the excited state ^{2}S.

Measuring the fluorescence emission resulting from the population of this upper state corresponds to the following operator $\hat{O}^{\mathrm{Ion}}$ expressed in the basis of the parent ion energy eigenstates as

$$\hat{O}^{\mathrm{Ion}} = \begin{pmatrix} -1 & 0 & 0 & 0 & & & & \\ 0 & -1 & 0 & 0 & & & & \\ 0 & 0 & -1 & 0 & & & & \\ 0 & 0 & 0 & +1 & & & & \\ & & & & -1 & 0 & 0 & 0 \\ & & & & 0 & -1 & 0 & 0 \\ & & & & 0 & 0 & -1 & 0 \\ & & & & 0 & 0 & 0 & +1 \end{pmatrix} \quad \text{(B2)}$$

The effective operator for the ionic measurement can be written as

$$\hat{Q}^{\mathrm{Ion}} = \hat{U}^{\dagger}\hat{O}^{\mathrm{Ion}}\hat{U}, \tag{B3}$$

$$\hat{U} = e^{-i\hat{H}^{\mathrm{I}}T}, \tag{B4}$$

where $\hat{U}$ is the unitary propagator constructed with the following interaction Hamiltonian, in the interaction picture:

$$\hat{H}^{\mathrm{I}} = \begin{pmatrix} H^{\mathrm{I}}_{AA} & 0 \\ 0 & H^{\mathrm{I}}_{BB} \end{pmatrix}, \tag{B5}$$

$$\hat{H}^{\mathrm{I}}_{AA} = \frac{1}{2}\begin{pmatrix} 0 & 0 & 0 & \Omega_a \\ 0 & 0 & 0 & iA_R\Omega_b e^{-i\phi_R} \\ 0 & 0 & 0 & iA_L\frac{\Omega_b}{\sqrt{3}}e^{-i\phi_L} \\ \Omega_a & -iA_R\Omega_b e^{i\phi_R} & -iA_L\frac{\Omega_b}{\sqrt{3}}e^{i\phi_L} & 0 \end{pmatrix}, \tag{B6}$$

$$\hat{H}^{\mathrm{I}}_{BB} = \frac{1}{2}\begin{pmatrix} 0 & 0 & 0 & iA_R\frac{\Omega_b}{\sqrt{3}}e^{-i\phi_R} \\ 0 & 0 & 0 & \Omega_a e^{-i\pi} \\ 0 & 0 & 0 & iA_L\Omega_b e^{-i\phi_L} \\ -iA_R\frac{\Omega_b}{\sqrt{3}}e^{i\phi_R} & \Omega_a e^{i\pi} & -iA_L\Omega_b e^{i\phi_L} & 0 \end{pmatrix}. \tag{B7}$$

This corresponds to two decoupled four-level systems. In Eqs. (B7) and (B8), $\Omega_a = E^{(1)}_{\mathrm{z}}d_A$ and $\Omega_b = E^{(2)}_{\mathrm{y}}d_B$ are the Rabi frequencies corresponding to the amplitudes of the two copropagating electric fields that are polarized along and perpendicular to the polarization direction of the photoionizing pulse, respectively. $A_R = +(1/\sqrt{2})$ and $A_L = +(1/\sqrt{2})$ are the amplitudes of the right-handed σ_- and left-handed σ_+ components of the linearly polarized $E^{(2)}_{\mathrm{y}}$ field, respectively. The phases ϕ_R and ϕ_L ($\phi_R = \phi_L$) are the phase differences between, respectively, the two circularly polarized components of the linearly polarized $E^{(2)}_{\mathrm{y}}$ field and the linearly polarized $E^{(1)}_{\mathrm{z}}$ field.

The $1/\sqrt{3}$ factor that differentiates the $\langle {}^2S_{1/2,+1/2}|\hat{H}^{\mathrm{I}}|{}^2P_{3/2,+3/2}\rangle$ and $\langle {}^2S_{1/2,-1/2}|\hat{H}^{\mathrm{I}}|{}^2P_{3/2,+1/2}\rangle$ Hamiltonian couplings in Eqs. (B7) and (B8), as also shown in Fig. 3, arise as follows:

$$d_B\frac{E^{(2)}_{\mathrm{y}}}{\sqrt{2}}e^{i\frac{\pi}{2}} = \langle {}^2S_{1/2,+1/2}|\hat{d}_{\mathrm{y}}E^{(2)}_{\mathrm{y}}|{}^2P_{3/2,+3/2}\rangle = +\langle {}^2S_{1/2,1/2}|\hat{d}_{\mathrm{y}}E^{(2)}_{\mathrm{y}}|{}^2P_{M_L=+1,M_S=+1/2}\rangle, \tag{B8}$$

$$\begin{aligned}\langle {}^2S_{1/2,-1/2}|\hat{d}_{\mathrm{y}}E^{(2)}_{\mathrm{y}}|{}^2P_{3/2,+1/2}\rangle &= +\sqrt{\frac{1}{3}}\langle {}^2S_{1/2,-1/2}|\hat{d}_{\mathrm{y}}E^{(2)}_{\mathrm{y}}|{}^2P_{M_L=+1,M_S=-1/2}\rangle + \sqrt{\frac{2}{3}}\langle {}^2S_{1/2,-1/2}|\hat{d}_{\mathrm{y}}E^{(2)}_{\mathrm{y}}|{}^2P_{M_L=0,M_S=+1/2}\rangle \\ &= +\frac{1}{\sqrt{3}}d_B\frac{E^{(2)}_{\mathrm{y}}}{\sqrt{2}}e^{i\frac{\pi}{2}}.\end{aligned} \tag{B9}$$

An analogous formula applies to the coupling matrix elements involving the states $|{}^2P_{3/2,-1/2}\rangle$ and $|{}^2P_{3/2,-3/2}\rangle$. The $e^{-i\pi} = -1$ factor that differentiates the $\langle {}^2S_{1/2,+1/2}|\hat{H}^{\mathrm{I}}|{}^2P_{1/2,+1/2}\rangle$ and $\langle {}^2S_{1/2,-1/2}|\hat{H}^{\mathrm{I}}|{}^2P_{1/2,-1/2}\rangle$ Hamiltonian couplings in Eqs. (B7) and (B8), as also shown in Fig. 3, arise as follows:

$$\begin{aligned}d_A E^{(1)}_{\mathrm{z}} &= \langle {}^2S_{1/2,+1/2}|\hat{d}_{\mathrm{z}}E^{(1)}_{\mathrm{z}}|{}^2P_{1/2,+1/2}\rangle \\ &= +\sqrt{\frac{2}{3}}\langle {}^2S_{1/2,+1/2}|\hat{d}_{\mathrm{z}}E^{(1)}_{\mathrm{z}}|{}^2P_{M_L=+1,M_S=-1/2}\rangle - \sqrt{\frac{1}{3}}\langle {}^2S_{1/2,+1/2}|\hat{d}_{\mathrm{z}}E^{(1)}_{\mathrm{z}}|{}^2P_{M_L=0,M_S=+1/2}\rangle \\ &= -\sqrt{\frac{1}{3}}\langle {}^2S_{1/2,+1/2}|\hat{d}_{\mathrm{z}}E^{(1)}_{\mathrm{z}}|{}^2P_{M_L=0,M_S=+1/2}\rangle,\end{aligned} \tag{B10}$$

$$\begin{aligned}\langle {}^2S_{1/2,-1/2}|\hat{d}_z E_z^{(1)}|{}^2P_{1/2,-1/2}\rangle &= +\sqrt{\frac{1}{3}}\langle {}^2S_{1/2,-1/2}|\hat{d}_z E_z^{(1)}|{}^2P_{M_L=0,M_S=-1/2}\rangle - \sqrt{\frac{2}{3}}\langle {}^2S_{1/2,-1/2}|\hat{d}_z E_z^{(1)}|{}^2P_{M_L=-1,M_S=+1/2}\rangle \\ &= +\sqrt{\frac{1}{3}}\langle {}^2S_{1/2,-1/2}|\hat{d}_z E_z^{(1)}|{}^2P_{M_L=0,M_S=-1/2}\rangle \\ &= -d_A E_z^{(1)}. \end{aligned} \tag{B11}$$

Diagonalization of the interaction Hamiltonian $\hat{H}^{\mathrm{I}}$ allows one to obtain a general form for the effective measurement operator on the parent ion subsystem expressed as

$$\hat{Q}^{\mathrm{Ion}} = \begin{pmatrix} Q_{11} & Q_{12} & Q_{15} & 0 & 0 & 0 \\ Q_{12}^* & Q_{22} & Q_{25} & 0 & 0 & 0 \\ Q_{15}^* & Q_{25}^* & Q_{55} & 0 & 0 & 0 \\ 0 & 0 & 0 & Q_{33} & Q_{34} & Q_{36} \\ 0 & 0 & 0 & Q_{34}^* & Q_{44} & Q_{46} \\ 0 & 0 & 0 & Q_{36}^* & Q_{46}^* & Q_{66} \end{pmatrix}, \tag{B12a}$$

where the matrix elements in the upper left block read as

$$Q_{11} = \frac{-\frac{2}{3}\Omega_b^2 - \Omega_a^2\cos(\sigma)}{\Omega_{\mathrm{eff}}^2}, \tag{B12b}$$

$$Q_{22} = -\frac{6\Omega_a^2 + \Omega_b^2[1+3\cos(\sigma)]}{6\Omega_{\mathrm{eff}}^2}, \tag{B12c}$$

$$Q_{55} = -\frac{6\Omega_a^2 + \Omega_b^2[3+\cos(\sigma)]}{6\Omega_{\mathrm{eff}}^2}, \tag{B12d}$$

$$Q_{12} = \frac{\sqrt{2}\Omega_a\Omega_b\sin^2(\frac{\sigma}{2})}{\Omega_{\mathrm{eff}}^2}e^{-i(\phi-\frac{\pi}{2})}, \tag{B12e}$$

$$Q_{15} = -\frac{\Omega_a\Omega_b[-1+\cos(\sigma)]}{\sqrt{6}\Omega_{\mathrm{eff}}^2}e^{-i(\phi-\frac{\pi}{2})}, \tag{B12f}$$

$$Q_{25} = -\frac{\sqrt{3}\Omega_b^2[-1+\cos(\sigma)]}{6\Omega_{\mathrm{eff}}^2}, \tag{B12g}$$

and the Ω_{eff} and σ parameters are given by

$$\Omega_{\mathrm{eff}} = \sqrt{\Omega_a^2 + \frac{2}{3}\Omega_b^2}; \qquad \sigma = \Omega_{\mathrm{eff}}T. \tag{B12h}$$

The matrix elements in the lower right block B (Q_{33}, Q_{34}, Q_{36}, Q_{44}, Q_{46} and Q_{66}) are related to the matrix elements of block A as follows:

$$Q_{33} = Q_{55} = -\frac{6\Omega_a^2 + \Omega_b^2[3+\cos(\sigma)]}{6\Omega_{\mathrm{eff}}^2}, \tag{B12i}$$

$$Q_{44} = Q_{11} = -\frac{2\Omega_b^2 + 3\Omega_a^2\cos(\sigma)}{3\Omega_{\mathrm{eff}}^2}, \tag{B12j}$$

$$Q_{66} = Q_{22} = -\frac{6\Omega_a^2 + \Omega_b^2[1+3\cos(\sigma)]}{6\Omega_{\mathrm{eff}}^2}, \tag{B12k}$$

$$Q_{34} = -Q_{15}^* = \frac{\Omega_a\Omega_b[-1+\cos(\sigma)]}{\sqrt{6}\Omega_{\mathrm{eff}}^2}e^{i(\phi-\frac{\pi}{2})}, \tag{B12l}$$

$$Q_{36} = Q_{25}^* = -\frac{\sqrt{3}\Omega_b^2[-1+\cos(\sigma)]}{6\Omega_{\mathrm{eff}}^2}, \tag{B12m}$$

$$Q_{46} = -Q_{12} = \frac{\Omega_a\Omega_b[-1+\cos(\sigma)]}{\sqrt{2}\Omega_{\mathrm{eff}}^2}e^{-i(\phi-\frac{\pi}{2})}. \tag{B12n}$$

Here we have included only the matrix elements of the $\hat{Q}$ operator in the Hilbert space of the parent ion that is initially populated by the ionizing pulse, i.e., excluding the $|{}^2S\rangle$ doublet.

The second ionic operator $\hat{R}^{\mathrm{Ion}}$ has the same structure and dependence on the parameters of the two laser pulses used as $\hat{Q}^{\mathrm{Ion}}$. The difference between the two operators is due to the different values of the laser parameters used in the corresponding ion manipulation scheme (see Fig. 3). By defining the following quantities as

$$\Omega_F = \frac{\Omega_b}{\Omega_a}, \qquad F = 6 + 4\Omega_F^2, \tag{B13}$$

we can write the parameter-dependent matrix elements of the ionic operators Q^{Ion} and R^{Ion} on the full space of ionic states, i.e., including the second excited ^{2}S state, as

$$Q/R^{\mathrm{Ion}} = \begin{pmatrix} (Q/R)^{\mathrm{Ion}}_{AA} & 0 \\ 0 & (Q/R)^{\mathrm{Ion}}_{BB} \end{pmatrix}, \tag{B14a}$$

$$(Q/R)^{\mathrm{Ion}}_{AA} = \frac{1}{F}\begin{pmatrix} -4\Omega_F^2 - 6\cos(\sigma) & 6\sqrt{2}\Omega_F \sin^2\left(\frac{\sigma}{2}\right)e^{-i(\phi-\frac{\pi}{2})} & \sqrt{6}\Omega_F[1-\cos(\sigma)]e^{-i(\phi-\frac{\pi}{2})} & i\sqrt{6F}\sin(\sigma) \\ 6\sqrt{2}\Omega_F \sin^2\left(\frac{\sigma}{2}\right)e^{i(\phi-\frac{\pi}{2})} & -6-\Omega_F^2[1+3\cos(\sigma)] & \sqrt{3}\Omega_F^2[1-\cos(\sigma)] & \sqrt{3F}\Omega_F\sin(\sigma)e^{i\phi} \\ \sqrt{6}\Omega_F[1-\cos(\sigma)]e^{i(\phi-\frac{\pi}{2})} & \sqrt{3}\Omega_F^2[1-\cos(\sigma)] & -6-\Omega_F^2[3+\cos(\sigma)] & \sqrt{F}\Omega_F\sin(\sigma)e^{i\phi} \\ -i\sqrt{6F}\sin(\sigma) & \sqrt{3F}\Omega_F\sin(\sigma)e^{-i\phi} & \sqrt{F}\Omega_F\sin(\sigma)e^{-i\phi} & F\cos(\sigma) \end{pmatrix}, \tag{B14b}$$

$$(Q/R)^{\mathrm{Ion}}_{BB} = \frac{1}{F}\begin{pmatrix} -6-\Omega_F^2[3+\cos(\sigma)] & \sqrt{6}\Omega_F[\cos(\sigma)-1]e^{i(\phi-\frac{\pi}{2})} & \sqrt{3}\Omega_F^2[1-\cos(\sigma)] & \sqrt{F}\Omega_F\sin(\sigma)e^{i\phi} \\ \sqrt{6}\Omega_F[\cos(\sigma)-1]e^{-i(\phi-\frac{\pi}{2})} & -4\Omega_F^2-6\cos(\sigma) & 6\sqrt{2}\Omega_F\sin^2\left(\frac{\sigma}{2}\right)e^{-i(\phi+\frac{\pi}{2})} & i\sqrt{6F}\sin(\sigma) \\ \sqrt{3}\Omega_F^2[1-\cos(\sigma)] & 6\sqrt{2}\Omega_F\sin^2\left(\frac{\sigma}{2}\right)e^{i(\phi+\frac{\pi}{2})} & -6-\Omega_F^2[1+3\cos(\sigma)] & \sqrt{3F}\Omega_F\sin(\sigma)e^{i\phi} \\ \sqrt{F}\Omega_F\sin(\sigma)e^{-i\phi} & i\sqrt{6F}\sin(\sigma) & \sqrt{3F}\Omega_F\sin(\sigma)e^{-i\phi} & F\cos(\sigma) \end{pmatrix}. \tag{B14c}$$

Evaluation of the two operators (by using the optimal parameters derived in Sec. III B for the case of postselection over the photoelectron emission direction) gives the following values for the noncommuting ionic operators:

$$Q^{\mathrm{Ion}}_{\mathrm{optimized}} = \frac{1}{10}\begin{pmatrix} 2 & -6\sqrt{2} & -2\sqrt{6} & 0 & & & & \\ -6\sqrt{2} & -4 & 2\sqrt{3} & 0 & & 0 & & \\ -2\sqrt{6} & 2\sqrt{3} & -8 & 0 & & & & \\ 0 & 0 & 0 & -10 & & & & \\ & & & & -8 & 2\sqrt{6} & 2\sqrt{3} & 0 \\ & 0 & & & 2\sqrt{6} & 2 & 6\sqrt{2} & 0 \\ & & & & 2\sqrt{3} & 6\sqrt{2} & -4 & 0 \\ & & & & 0 & 0 & 0 & -10 \end{pmatrix}, \tag{B15}$$

$$R^{\mathrm{Ion}}_{\mathrm{optimized}} = \frac{1}{22}\begin{pmatrix} -10 & -12\sqrt{2} & -4\sqrt{6} & 0 & & & & \\ -12\sqrt{2} & 2 & 8\sqrt{3} & 0 & & 0 & & \\ -4\sqrt{6} & 8\sqrt{3} & -14 & 0 & & & & \\ 0 & 0 & 0 & -22 & & & & \\ & & & & -14 & 4\sqrt{6} & 8\sqrt{3} & 0 \\ & 0 & & & 4\sqrt{6} & -10 & 12\sqrt{2} & 0 \\ & & & & 8\sqrt{3} & 12\sqrt{2} & 2 & 0 \\ & & & & 0 & 0 & 0 & -22 \end{pmatrix}. \tag{B16}$$

Using this type of measurement for the parent ion subsystem combined with the spin measurements for the photoelectron, we can write the following Bell inequality:

$$\mathbb{S} = \langle \hat{Q}^{\mathrm{Ion}} \otimes 2\hat{S}_x \rangle + \langle \hat{Q}^{\mathrm{Ion}} \otimes 2\hat{S}_z \rangle + \langle \hat{R}^{\mathrm{Ion}} \otimes 2\hat{S}_x \rangle - \langle \hat{R}^{\mathrm{Ion}} \otimes 2\hat{S}_z \rangle. \tag{B17}$$

Since both the ionic and the photoelectron operators defined above have eigenvalues equal to ± 1, the condition for detection of quantum entanglement between the photoelectron and the parent ion reads as

$$\mathbb{S} \geq 2. \tag{B18}$$

The operators acting on the composite bipartite system read as

$$\hat{Q}^{\mathrm{Ion}} \otimes 2\hat{S}_z = \begin{pmatrix} +Q_{11} & 0 & 0 & 0 & 0 & 0 \\ 0 & -Q_{22} & 0 & 0 & 0 & 0 \\ 0 & 0 & -Q_{55} & 0 & 0 & 0 \\ 0 & 0 & 0 & +Q_{33} & 0 & 0 \\ 0 & 0 & 0 & 0 & -Q_{44} & 0 \\ 0 & 0 & 0 & 0 & 0 & +Q_{66} \end{pmatrix} \tag{B19}$$

and

$$\hat{Q}^{\mathrm{Ion}} \otimes 2\hat{S}_x = \begin{pmatrix} 0 & Q_{12} & Q_{15} & 0 & 0 & 0 \\ Q_{12}^* & 0 & Q_{25} & 0 & 0 & 0 \\ Q_{15}^* & Q_{25}^* & 0 & 0 & 0 & 0 \\ 0 & 0 & 0 & 0 & Q_{34} & Q_{36} \\ 0 & 0 & 0 & Q_{34}^* & 0 & Q_{46} \\ 0 & 0 & 0 & Q_{36}^* & Q_{46}^* & 0 \end{pmatrix}. \tag{B20}$$

Using the density matrix in Eq. (B1) to compute the traces, we finally obtain

$$\begin{aligned} \mathbb{S} = {} & +Q_{11}|\tilde{C}_{1,\uparrow}(\xi)|^2 - Q_{22}|\tilde{C}_{2,\downarrow}(\xi)|^2 - Q_{55}|\tilde{C}_{5,\downarrow}(\xi)|^2 + Q_{33}|\tilde{C}_{3,\uparrow}(\xi)|^2 - Q_{44}|\tilde{C}_{4,\downarrow}(\xi)|^2 + Q_{66}|\tilde{C}_{6,\uparrow}(\xi)|^2 \\ & - (R_{11}|\tilde{C}_{1,\uparrow}(\xi)|^2 - R_{22}|\tilde{C}_{2,\downarrow}(\xi)|^2 - R_{55}|\tilde{C}_{5,\downarrow}(\xi)|^2 + R_{33}|\tilde{C}_{3,\uparrow}(\xi)|^2 - R_{44}|\tilde{C}_{4,\downarrow}(\xi)|^2 + R_{66}|\tilde{C}_{6,\uparrow}(\xi)|^2) \\ & + 2\mathrm{Re}[Q_{12}\tilde{\rho}^*_{1\uparrow,2\downarrow}(\xi) + R_{12}\tilde{\rho}^*_{1\uparrow,2\downarrow}(\xi) + Q_{15}\tilde{\rho}^*_{1\uparrow,5\downarrow}(\xi) + R_{15}\tilde{\rho}^*_{1\uparrow,5\downarrow}(\xi) + Q_{25}\tilde{\rho}^*_{2\downarrow,5\downarrow}(\xi) + R_{25}\tilde{\rho}^*_{2\downarrow,5\downarrow}(\xi)] \\ & + 2\mathrm{Re}[Q_{34}\tilde{\rho}^*_{3\uparrow,4\downarrow}(\xi) + R_{34}\tilde{\rho}^*_{3\uparrow,4\downarrow}(\xi) + Q_{36}\tilde{\rho}^*_{3\uparrow,6\uparrow}(\xi) + R_{36}\tilde{\rho}^*_{3\uparrow,6\uparrow}(\xi) + Q_{46}\tilde{\rho}^*_{4\downarrow,6\uparrow}(\xi) + R_{46}\tilde{\rho}^*_{4\downarrow,6\uparrow}(\xi)]. \end{aligned} \tag{B21}$$

[1] R. Horodecki, P. Horodecki, M. Horodecki, and K. Horodecki, *Quantum entanglement*, Rev. Mod. Phys. **81**, 865 (2009).

[2] M. A. Nielsen and I. L. Chuang, *Quantum Computation and Quantum Information*, 10th ed. (Cambridge University Press, Cambridge, England, 2010).

[3] S. Steinlechner, J. Bauchrowitz, M. Meinders, H. Muller-Ebhardt, K. Danzmann, and R. Schnabel, *Quantum-dense metrology*, Nat. Photonics **7**, 626 (2013).

[4] C. L. Degen, F. Reinhard, and P. Cappellaro, *Quantum sensing*, Rev. Mod. Phys. **89**, 035002 (2017).

[5] K. Bongs, M. Holynski, J. Vovrosh, P. Bouyer, G. Condon, E. Rasel, C. Schubert, W. P. Schleich, and A. Roura, *Taking atom interferometric quantum sensors from the laboratory to real-world applications*, Nat. Rev. Phys. **1**, 731 (2019).

[6] H. Defienne, B. Ndagano, A. Lyons, and D. Faccio, *Polarization entanglement-enabled quantum holography*, Nat. Phys. **17**, 591 (2021).

[7] T. Radtke, A. Surzhykov, and S. Fritzsche, *Photon pairs with tailor-made entanglement obtained from the two-photon decay of atomic hydrogen*, Phys. Rev. A **77**, 022507 (2008).

[8] F. Fratini, M. C. Tichy, T. Jahrsetz, A. Buchleitner, S. Fritzsche, and A. Surzhykov, *Quantum correlations in the two-photon decay of few-electron ions*, Phys. Rev. A **83**, 032506 (2011).

[9] M. C. Tichy, F. Mintert, and A. Buchleitner, *Essential entanglement for atomic and molecular physics*, J. Phys. B **44**, 192001 (2011).

[10] F. Krausz and M. Ivanov, *Attosecond physics*, Rev. Mod. Phys. **81**, 163 (2009).

[11] S. R. Leone, C. W. McCurdy, J. Burgdörfer, L. S. Cederbaum, Z. Chang, N. Dudovich, J. Feist, C. H. Greene, M. Ivanov, R. Kienberger, U. Keller, M. F. Kling, Z.-H. Loh, T. Pfeifer, A. N. Pfeiffer, R. Santra, K. Schafer, A. Stolow, U. Thumm, and M. J. J. Vrakking, *What will it take to observe processes in 'real time'?*, Nat. Photonics **8**, 162 (2014).

[12] F. Calegari, G. Sansone, S. Stagira, C. Vozzi, and M. Nisoli, *Advances in attosecond science*, J. Phys. B **49**, 062001 (2016).

[13] J. Itatani, J. Levesque, D. Zeidler, H. Niikura, H. Pepin, J. C. Kieffer, P. B. Corkum, and D. M. Villeneuve, *Tomographic imaging of molecular orbitals*, Nature (London) **432**, 867 (2004).

[14] H. Niikura, F. Legare, R. Hasbani, A. D. Bandrauk, M. Y. Ivanov, D. M. Villeneuve, and P. B. Corkum, *Sub-laser-cycle electron pulses for probing molecular dynamics*, Nature (London) **417**, 917 (2002).

[15] Y. Huismans *et al.*, *Time-resolved holography with photoelectrons*, Science **331**, 61 (2011).

[16] J. Itatani, F. Quere, G. L. Yudin, M. Y. Ivanov, F. Krausz, and P. B. Corkum, *Attosecond streak camera*, Phys. Rev. Lett. **88**, 173903 (2002).

[17] F. Calegari, D. Ayuso, A. Trabattoni, L. Belshaw, S. D. Camillis, S. Anumula, F. Frassetto, L. Poletto, A. Palacios, P. Decleva, J. B. Greenwood, F. Martin, and M. Nisoli, *Ultrafast electron dynamics in phenylalanine initiated by attosecond pulses*, Science **346**, 336 (2014).

[18] T. Barillot *et al.*, *Correlation-driven transient hole dynamics resolved in space and time in the isopropanol molecule*, Phys. Rev. X **11**, 031048 (2021).

[19] D. Schwickert *et al.*, *Electronic quantum coherence in glycine molecules probed with ultrashort x-ray pulses in real time*, Sci. Adv. **8**, eabn6848 (2022).

[20] A. S. Johnson, D. R. Austin, D. A. Wood, C. Brhamsan, D. Gregory, K. B. Holzner, S. Jarosch, E. W. Larsen, S. Parker, C. S. Struber, P. Ye, J. W. G. Tisch, and J. P. Marangos, *High-flux soft x-ray harmonic generation from ionization-shaped few-cycle laser pulses*, Sci. Adv. **4**, eaar3761 (2018).

[21] J. Duris *et al.*, *Tunable isolated attosecond x-ray pulses with gigawatt peak power from a free-electron laser*, Nat. Photonics **14**, 30 (2020).

[22] T. Radtke, S. Fritzsche, and A. Surzhykov, *Density matrix formalism for the photoion-electron entanglement in atomic photoionization*, Phys. Rev. A **74**, 032709 (2006).

[23] D. Akoury *et al.*, *The simplest double slit: Interference and entanglement in double photoionization of* H_2, Science **318**, 949 (2007).

[24] M. S. Schöffler *et al.*, *Ultrafast probing of core hole localization in* N_2, Science **320**, 920 (2008).

[25] E. Goulielmakis, Z.-H. Loh, A. Wirth, R. Santra, N. Rohringer, V. S. Yakovlev, S. Zherebtsov, T. Pfeifer, A. M. Azzeer, M. F. Kling, S. R. Leone, and F. Krausz, *Real-time observation of valence electron motion*, Nature (London) **466**, 739 (2010).

[26] M. Ruberti, *Onset of ionic coherence and ultrafast charge dynamics in attosecond molecular ionisation*, Phys. Chem. Chem. Phys. **21**, 17584 (2019).

[27] M. J. J. Vrakking, *Control of attosecond entanglement and coherence*, Phys. Rev. Lett. **126**, 113203 (2021).

[28] L.-M. Koll, L. Maikowski, L. Drescher, T. Witting, and M. J. J. Vrakking, *Experimental control of quantum-mechanical entanglement in an attosecond pump-probe experiment*, Phys. Rev. Lett. **128**, 043201 (2022).

[29] M. Ruberti, *Quantum electronic coherences by attosecond transient absorption spectroscopy: Ab initio B-spline RCS-ADC study*, Faraday Discuss. **228**, 286 (2021).

[30] M. Ruberti, S. Patchkovskii, and V. Averbukh, *Quantum coherence in molecular photoionization*, Phys. Chem. Chem. Phys. **24**, 19673 (2022).

[31] O. G. Alexander, J. P. Marangos, M. Ruberti, and M. Vacher, *Attosecond electron dynamics in molecular systems*, in *Advances in Atomic, Molecular and Optical Physics*, edited by L. F. DiMauro, H. Perrin, and S. F. Yelin (Elsevier Academic Press, New York, 2023), Vol. 72, pp. 183–252.

[32] C. Bourassin-Bouchet, L. Barreau, V. Gruson, J.-F. Hergott, F. Quere, P. Salieres, and T. Ruchon, *Quantifying decoherence in attosecond metrology*, Phys. Rev. X **10**, 031048 (2020).

[33] J. Breidbach and L. S. Cederbaum, *Migration of holes: Formalism, mechanisms, and illustrative applications*, J. Chem. Phys. **118**, 3983 (2003).

[34] A. I. Kuleff and L. S. Cederbaum, *Ultrafast correlation-driven electron dynamics*, J. Phys. B **47**, 124002 (2014).

[35] V. Despré, A. Marciniak, V. Loriot, M. C. E. Galbraith, A. Rouzée, M. J. J. Vrakking, F. Lépine, and A. I. Kuleff, *Attosecond hole migration in benzene molecules surviving nuclear motion*, J. Phys. Chem. Lett. **6**, 426 (2015).

[36] A. I. Kuleff, N. V. Kryzhevoi, M. Pernpointner, and L. S. Cederbaum, *Core ionization initiates subfemtosecond charge migration in the valence shell of molecules*, Phys. Rev. Lett. **117**, 093002 (2016).

[37] H. Du, C. Covington, S. R. Leone, and K. Varga, *Excited-state electronic coherence in vinyl bromide ions*, Phys. Rev. A **100**, 053412 (2019).

[38] D. T. Matselyukh, V. Despre, N. V. Golubev, A. I. Kuleff, and H. J. Wörner, *Decoherence and revival in attosecond charge migration driven by non-adiabatic dynamics*, Nat. Phys. **18**, 1206 (2022).

[39] Y. Gu, B. Gu, S. Sun, H. Yong, V. Y. Chernyak, and S. Mukamel, *Manipulating attosecond charge migration in molecules by optical cavities*, J. Am. Chem. Soc. **145**, 14856 (2023).

[40] A. Niehaus, *Analysis of post-collision interactions in Auger processes following near-threshold inner-shell photoionization*, J. Phys. B **10**, 1845 (1977).

[41] W. Eberhardt, S. Bernstorff, H. W. Jochims, S. B. Whitfield, and B. Crasemann, *Photoelectron recapture through post-collision interaction*, Phys. Rev. A **38**, 3808 (1988).

[42] R. Guillemin, S. Sheinerman, R. Püttner, T. Marchenko, G. Goldsztejn, L. Journel, R. K. Kushawaha, D. Céolin, M. N. Piancastelli, and M. Simon, *Postcollision interaction effects in KLL Auger spectra following argon* 1*s photoionization*, Phys. Rev. A **92**, 012503 (2015).

[43] B. Schmidtke, M. Drescher, N. A. Cherepkov, and U. Heinzmann, *On the impossibility to perform a complete*

valence-shell photoionization experiment with closed-shell atoms, J. Phys. B **33**, 2451 (2000).

[44] G. Snell, U. Hergenhahn, N. Muller, M. Drescher, J. Viefhaus, U. Becker, and U. Heinzmann, *Study of xenon* 4*d*, 5*p*, *and* 5*s photoionization in the shape-resonance region using spin-resolved electron spectroscopy*, Phys. Rev. A **63**, 032712 (2001).

[45] M. V. Fedorov, M. A. Efremov, A. E. Kazakov, K. W. Chan, C. K. Law, and J. H. Eberly, *Packet narrowing and quantum entanglement in photoionization and photodissociation*, Phys. Rev. A **69**, 052117 (2004).

[46] N. Chandra and R. Ghosh, *Entanglement in double photoionization of rotating linear molecules*, Phys. Rev. A **69**, 012315 (2004).

[47] Y. S. Kim, Y. J. Kim, and R. H. Pratt, *Entanglement change in atomic photoionization*, Phys. Scr. **T110**, 79 (2004).

[48] M. Spanner and P. Brumer, *Entanglement and timing-based mechanisms in the coherent control of scattering processes*, Phys. Rev. A **76**, 013408 (2007).

[49] M. Spanner and P. Brumer, *Coherent control and entanglement in the attosecond electron-recollision dissociation of* D_2^+, Phys. Rev. A **76**, 013409 (2007).

[50] M. Vatasescu, *Entanglement between electronic and vibrational degrees of freedom in a laser-driven molecular system*, Phys. Rev. A **88**, 063415 (2013).

[51] S. M. A. Czirjak, J. Kovacs, and M. G. Benedict, *Emergence of oscillations in quantum entanglement during rescattering*, Phys. Scr. **T153**, 014013 (2013).

[52] M. Chakraborty and S. Sen, *Entanglement of mixed quantum states for qubits and qudit in double photoionization of atoms*, J. Electron Spectrosc. Relat. Phenom. **203**, 60 (2015).

[53] S. Majorosi, M. G. Benedict, and A. Czirjak, *Quantum entanglement in strong-field ionization*, Phys. Rev. A **96**, 043412 (2017).

[54] T. Nishi, E. Lötstedt, and K. Yamanouchi, *Entanglement and coherence in photoionization of* H_2 *by an ultrashort XUV laser pulse*, Phys. Rev. A **100**, 013421 (2019).

[55] M. J. J. Vrakking, *Ion-photoelectron entanglement in photoionization with chirped laser pulses*, J. Phys. B **55**, 134001 (2022).

[56] S. Nandi *et al.*, *Generation of entanglement using a short-wavelength seeded free-electron laser*, Sci. Adv. **10**, eado0668 (2024).

[57] W.-C. Liu, J. H. Eberly, S. L. Haan, and R. Grobe, *Correlation effects in two-electron model atoms in intense laser fields*, Phys. Rev. Lett. **83**, 520 (1999).

[58] I. P. Christov, *Phase-locking mechanism in non-sequential double ionization*, Appl. Phys. B **125**, 209 (1999).

[59] J. J. Omiste and L. B. Madsen, *Effects of core space and excitation levels on ground-state correlation and photoionization dynamics of* Be *and* Ne, J. Chem. Phys. **150**, 084305 (2019).

[60] A. S. Maxwell, L. B. Madsen, and M. Lewenstein, *Entanglement of orbital angular momentum in non-sequential double ionization*, Nat. Commun. **13**, 4706 (2022).

[61] S. Eckart, D. Trabert, J. Rist, A. Geyer, L. P. H. Schmidt, K. Fehre, and M. Kunitski, *Ultrafast preparation and detection of entangled atoms*, Sci. Adv. **9**, eabq8227 (2023).

[62] F. Shobeiry, P. Fross, H. Srinivas, T. Pfeifer, R. Moshammer, and A. Harth, *Sub-femtosecond optical control of entangled states*, arXiv:2110.06668.

[63] J. S. Bell, *On the Einstein Podolsky Rosen paradox*, Physics (Long Island City, N.Y.) **1**, 195 (1964).

[64] C. A. Kocher and E. D. Commins, *Polarization correlation of photons emitted in an atomic cascade*, Phys. Rev. Lett. **18**, 575 (1967).

[65] J.-W. Pan, D. Bouwmeester, M. Daniell, H. Weinfurter, and A. Zeilinger, *Experimental test of quantum nonlocality in three-photon Greenberger-Horne-Zeilinger entanglement*, Nature (London) **403**, 515 (2000).

[66] K. C. Lee, M. R. Sprague, B. J. Sussman, J. Nunn, N. K. Langford, X.-M. Jin, T. Champion, P. Michelberger, K. F. Reim, D. England, D. Jaksch, and I. A. Walmsley, *Entangling macroscopic diamonds at room temperature*, Science **334**, 1253 (2011).

[67] B. Hensen, H. Bernien, A. E. Dreau, A. Reiserer, N. Kalb, M. S. Blok, J. Ruitenberg, R. F. L. Vermeulen, R. N. Schouten, C. Abellan, W. Amaya, V. Pruneri, M. W. Mitchell, M. Markham, D. J. Twitchen, D. Elkouss, S. Wehner, T. H. Taminiau, and R. Hanson, *Loophole-free Bell inequality violation using electron spins separated by 1.3 kilometres*, Nature (London) **526**, 682 (2015).

[68] F. Clauser, M. A. Horne, A. Shimony, and R. A. Holt, *Proposed experiment to test local hidden-variable theories*, Phys. Rev. Lett. **23**, 880 (1969).

[69] B. S. Cirel'son, *Quantum generalizations of Bell's inequality*, Lett. Math. Phys. **4**, 93 (1980).

[70] T. R. Harvey, V. Grillo, and B. J. McMorran, *Stern-Gerlach-like approach to electron orbital angular momentum measurement*, Phys. Rev. A **95**, 021801(R) (2017).

[71] V. Grillo, A. H. Tavabi, F. Venturi, H. Larocque, R. Balboni, G. Gazzadi, S. Frabboni, P.-H. Lu, E. Mafakheri, F. Bouchard, R. E. Dunin-Borkowski, R. W. Boyd, M. P. J. Lavery, M. J. Padgett, and E. Karimi, *Measuring the orbital angular momentum spectrum of an electron beam*, Nat. Commun. **8**, 15536 (2017).

[72] H. Larocque, I. Kaminer, V. Grillo, G. Leuchs, M. J. Padgett, R. W. Boyd, M. Segev, and E. Karimi, *'Twisted' electrons*, Contemp. Phys. **59**, 126 (2018).

[73] A. Hartung, F. Morales, M. Kunitski, K. Henrichs, A. Laucke, M. Richter, T. Jahnke, A. Kalinin, M. Schöffler, L. P. H. Schmidt, M. Ivanov, O. Smirnova, and R. Dörner, *Electron spin polarization in strong-field ionization of xenon atoms*, Nat. Photonics **10**, 526 (2016).

[74] D. Trabert, A. Hartung, S. Eckart, F. Trinter, A. Kalinin, M. Schöffler, L. P. H. Schmidt, T. Jahnke, M. Kunitski, and R. Dörner, *Spin and angular momentum in strong field ionization*, Phys. Rev. Lett. **120**, 043202 (2018).

[75] R. Berezov, J. Jacoby, and J. Schunk, *Spin coincidence measurements for a symmetric scattering of electrons with electrons*, Nucl. Instrum. Methods Phys. Res., Sect. A **621**, 673 (2010).

[76] G. C. Burnett, T. J. Monroe, and F. B. Dunning, *High-efficiency retarding-potential Mott polarization analyzer*, Rev. Sci. Instrum. **65**, 1893 (1994).

[77] O. E. Tereshchenko, V. A. Golyashov, V. S. Rusetsky, A. V. Mironov, A. Y. Demin, and V. V. Aksenov, *A new imaging concept in spin polarimetry based on the spin-filter effect*, J. Synchrotron Radiat. **28**, 864 (2021).

[78] C. Bigi, P. K. Das, D. Benedetti, F. Salvador, D. Krizmancic, R. Sergo, A. Martin, G. Panaccione, G. Rossi, J. Fujii, and I. Vobornik, *Very efficient spin polarization analysis (VESPA): New exchange scattering-based setup for spin-resolved ARPES at APE-NFFA beamline at Elettra*, J. Synchrotron Radiat. **24**, 750 (2017).

[79] R. Bertacco, M. Marcon, G. Trezzi, L. Duo, and F. Ciccacci, *Spin and energy analysis of electron beams: Coupling a polarimeter based on exchange scattering to a hemispherical analyzer*, Rev. Sci. Instrum. **73**, 3867 (2002).

[80] C. Jozwiak, J. Graf, G. Lebedev, N. Andresen, A. Schmid, A. Fedorov, F. E. Gabaly, W. Wan, A. Lanzara, and Z. Hussain, *A high-efficiency spin-resolved photoemission spectrometer combining time-of-flight spectroscopy with exchange-scattering polarimetry*, Rev. Sci. Instrum. **81**, 053904 (2010).

[81] D. Kutnyakhov *et al.*, *Imaging spin filter for electrons based on specular reflection from iridium (001)*, Ultramicroscopy **130**, 63 (2013).

[82] K. Kawaguchi, K. Kuroda, Z. Zhao, S. Tani, A. Harasawa, Y. Fukushima, H. Tanaka, R. Noguchi, T. Iimori, K. Yaji, M. Fujisawa, S. Shin, F. Komori, Y. Kobayashi, and T. Kondo, *Time-, spin-, and angle-resolved photoemission spectroscopy with a 1-MHz 10.7-eV pulse laser*, Rev. Sci. Instrum. **94**, 083902 (2023).

[83] I. Barth and O. Smirnova, *Spin-polarized electrons produced by strong-field ionization*, Phys. Rev. A **88**, 013401 (2013).

[84] I. Barth and M. Lein, *Numerical verification of the theory of nonadiabatic tunnel ionization in strong circularly polarized laser fields*, J. Phys. B **47**, 204016 (2014).

[85] T. Herath, L. Yan, S. K. Lee, and W. Li, *Strong-field ionization rate depends on the sign of the magnetic quantum number*, Phys. Rev. Lett. **109**, 043004 (2012).

[86] M.-M. Liu, Y. Shao, M. Han, P. Ge, Y. Deng, C. Wu, Q. Gong, and Y. Liu, *Energy- and momentum-resolved photoelectron spin polarization in multiphoton ionization of* Xe *by circularly polarized fields*, Phys. Rev. Lett. **120**, 043201 (2018).

[87] N. A. Cherepkov, *Theory of spin polarisation phenomena in molecular photoionisation processes*, J. Phys. B **14**, 2165 (1981).

[88] U. Fano, *Spin orientation of photoelectrons ejected by circularly polarized light*, Phys. Rev. **178**, 131 (1969).

[89] P. Lambropoulos, *Spin-orbit coupling and photoelectron polarization in multiphoton ionization of atoms*, Phys. Rev. Lett. **30**, 413 (1973).

[90] S. N. Dixit, P. Lambropoulos, and P. Zoller, *Spin polarization of electrons in two-photon resonant three-photon ionization*, Phys. Rev. A **24**, 318 (1981).

[91] M. R. Teague and P. Lambropoulos, *Three-photon ionization with spin-orbit coupling*, J. Phys. B **9**, 1251 (1976).

[92] T. Nakajima and P. Lambropoulos, *Electron spin-polarization in single-, two- and three-photon ionization of xenon*, Europhys. Lett. **57**, 25 (2002).

[93] I. Barth and O. Smirnova, *Nonadiabatic tunneling in circularly polarized laser fields: Physical picture and calculations*, Phys. Rev. A **84**, 063415 (2011).

[94] S. Eckart, M. Kunitski, M. Richter, A. Hartung, J. Rist, F. Trinter, K. Fehre, N. Schlott, K. Henrichs, L. Schmidt, T. Jahnke, M. Schöffler, K. Liu, I. Barth, J. Kaushal, F. Morales, M. Ivanov, O. Smirnova, and R. Dörner, *Ultrafast preparation and detection of ring currents in single atoms*, Nat. Phys. **14**, 701 (2018).

[95] M. Lukin, *Colloquium: Trapping and manipulating photon states in atomic ensembles.*, Rev. Mod. Phys. **75**, 457 (2003).

[96] M. Ruberti, V. Averbukh, and P. Decleva, *B-spline algebraic diagrammatic construction: Application to photoionization cross-sections and high-order harmonic generation*, J. Chem. Phys. **141**, 164126 (2014).

[97] V. Averbukh and M. Ruberti, *First-principles many-electron dynamics using the B-spline algebraic diagrammatic construction approach*, in *Attosecond Molecular Dynamics*, Theoretical and Computational Chemistry Series Vol. 13, edited by M. Vrakking and F. Lepine (Royal Society Chemistry, Cambridge, 2018), pp. 68–102.

[98] M. Ruberti, *Restricted correlation space B-spline ADC approach to molecular ionization: Theory and applications to total photoionization cross-sections*, J. Chem. Theory Comput. **15**, 3635 (2019).

[99] M. Ruberti and V. Averbukh, *Advances in modeling attosecond electron dynamics in molecular photoionization*, WIREs Comput. Mol. Sci. **13**, e1673 (2023).

[100] M. Ruberti, P. Decleva, and V. Averbukh, *Full ab initio many-electron simulation of attosecond molecular pump–probe spectroscopy*, J. Chem. Theory Comput. **14**, 4991 (2018).

[101] D. You *et al.*, *A detailed investigation of single-photon laser enabled Auger decay in neon*, New J. Phys. **21**, 113036 (2019).

[102] M. Ruberti, P. Decleva, and V. Averbukh, *Multi-channel dynamics in high harmonic generation of aligned* CO_2*: Ab initio analysis with time-dependent B-spline algebraic diagrammatic construction*, Phys. Chem. Chem. Phys. **20**, 8311 (2018).

[103] A. Bray, A. S. Maxwell, Y. Kissin, M. Ruberti, M. F. Ciappina, V. Averbukh, and C. F. D. M. Faria, *Polarization in strong-field ionization of excited helium*, J. Phys. B **54**, 194002 (2021).

[104] P. Eckle, M. Smolarski, P. Schlup, J. Biegert, A. Staudte, M. Schöffler, H. Muller, R. Dörner, and U. Keller, *Attosecond angular streaking*, Nat. Phys. **4**, 565 (2008).

[105] P. Eckle, A. Pfeiffer, C. Cirelli, A. Staudte, R. Dörner, H. G. Muller, M. Buttiker, and U. Keller, *Attosecond ionization and tunneling delay time measurements in helium*, Science **322**, 1525 (2020).

[106] L. Torlina, F. Morales, J. Kaushal, I. Ivanov, A. Kheifets, A. Zielinski, A. Scrinzi, H. Muller, S. Sukiasyan, M. Ivanov, and O. Smirnova, *Interpreting attoclock measurements of tunnelling times*, Nat. Phys. **11**, 503 (2020).

[107] A. Hans, C. Ozga, P. Schmidt, G. Hartmann, A. Nehls, P. Wenzel, C. Richter, C. Lant, X. Holzapfel, J. Viehmann, U. Hergenhahn, A. Ehresmann, and A. Knie, *Setup for multicoincidence experiments of photons in the extreme ultraviolet to visible spectral range and charged*

particles—the solid angle maximization approach, Rev. Sci. Instrum. **90**, 093104 (2019).

[108] A. Hans, T. Miteva, X. Holzapfel, C. Ozga, P. Schmidt, H. Otto, G. Hartmann, C. Richter, N. Sisourat, A. Ehresmann, K. Gokhberg, U. Hergenhahn, and A. Knie, *Electronic decay of singly charged ground-state ions by charge transfer via van der Waals bonds*, Phys. Rev. Lett. **123**, 213001 (2019).

[109] A. Hans, C. Kustner-Wetekam, P. Schmidt, C. Ozga, X. Holzapfel, H. Otto, C. Zindel, C. Richter, L. S. Cederbaum, A. Ehresmann, U. Hergenhahn, N. V. Kryzhevoi, and A. Knie, *Core-level interatomic Coulombic decay in van der Waals clusters*, Phys. Rev. Res. **2**, 012022(R) (2020).

[110] A. Hans, N. Kiefer, L. Marder, C. Kustner-Wetekam, E. Heikura, N. Golchert, J. H. Viehmann, D. Cubaynes, I. Ismail, F. Trinter, P. Lablanquie, J. Palaudoux, A. Ehresmann, and F. Penent, *Experimental realization of Auger decay in the field of a positive elementary charge*, Phys. Rev. Lett. **132**, 203002 (2024).

[111] H. Srinivas, F. Shobeiry, D. Bharti, T. Pfeifer, R. Moshammer, and A. Harth, *High-repetition rate attosecond beamline for multi-particle coincidence experiments*, Opt. Express **30**, 13630 (2022).

[112] S. Mikaelsson, J. Vogelsang, C. Guo, I. Sytcevich, A.-L. Viotti, F. Langer, Y.-C. Cheng, S. Nandi, W. Jin, A. Olofsson, R. Weissenbilder, J. Mauritsson, A. L'Huillier, M. Gisselbrecht, and C. L. Arnold, *A high-repetition rate attosecond light source for time-resolved coincidence spectroscopy*, Nanophotonics **10**, 117 (2021).

[113] S. J. Freedman and J. F. Clauser, *Experimental test of local hidden-variable theories*, Phys. Rev. Lett. **28**, 938 (1972).

[114] A. Aspect, J. Dalibard, and G. Roger, *Experimental test of Bell's inequalities using time-varying analyzers*, Phys. Rev. Lett. **49**, 1804 (1982).

[115] G. Weihs, T. Jennewein, C. Simon, H. Weinfurter, and A. Zeilinger, *Violation of Bell's inequality under strict Einstein locality conditions*, Phys. Rev. Lett. **81**, 5039 (1998).

[116] W. Wiese, M. Smith, and B. Miles, *Atomic transition probabilities, volume II. sodium through calcium—a critical data compilation*, National Institute of Standards and Technology, Gaithersburg, MD (1969), 10.6028/NBS.NSRDS.22.

[117] M. Kretschmar, M. Vrakking, and B. Schutte, *Intense XUV pulses from a compact HHG setup using a single harmonic*, J. Phys. B **54**, 20LT01 (2021).

[118] S. Nandi *et al.*, *Observation of Rabi dynamics with a short-wavelength free-electron laser*, Nature (London) **608**, 488 (2022).